

Banner appropriate to article type will appear here in typeset article

An empirical model of noise sources in subsonic jets

U. Karban¹†, B. Bugeat², A. Towne³, L. Lesshafft⁴, A. Agarwal², P. Jordan⁵

¹Department of Aerospace Engineering, Middle East Technical University, Ankara, Turkey

²Department of Engineering, Trumpington St, Cambridge CB2 1PZ, U.K.

³Department of Mechanical Engineering, University of Michigan, Ann Arbor, MI 48109, USA

⁴Laboratoire d'Hydrodynamique, CNRS / École polytechnique, Institut Polytechnique de Paris, Palaiseau, France

⁵Département Fluides, Thermique, Combustion, Institut PPrime, CNRS-University of Poitiers-ENSMA, France

(Received xx; revised xx; accepted xx)

Modelling the noise emitted by turbulent jets is made difficult by their acoustic inefficiency: only a tiny fraction of the near-field turbulent kinetic energy is propagated to the far field as acoustic waves. As a result, jet-noise models must accurately capture this small, acoustically efficient component hidden among comparatively inefficient fluctuations. In this paper, we identify this acoustically efficient near-field source from large-eddy-simulation data and use it to inform a predictive model. Our approach uses the resolvent framework, in which the source takes the form of nonlinear fluctuation terms that act as a forcing on the linearized Navier-Stokes equations. First, we identify the forcing that, when acted on by the resolvent operator, produces the leading spectral proper orthogonal decomposition modes in the acoustic field for a Mach 0.4 jet. Second, the radiating components of this forcing are isolated by retaining only portions with a supersonic phase speed. This component makes up less than 0.05% of the total forcing energy but generates most of the acoustic response, especially at peak (downstream) radiation angles. Finally, we propose an empirical model for the identified acoustically efficient forcing components. The model is tested at other Mach numbers and flight-stream conditions and predicts noise within 2 dB accuracy for a range of frequencies, downstream angles, and flight conditions.

Key words: ...

1. Introduction

Jet noise is one of the most studied problems in aeroacoustics, thanks largely to Lighthill's theoretical framework that allows a connection to be made between the stochastic, nonlinear, vortical motions of a turbulent jet and the irrotational, linear fluctuations of the resulting acoustic field (Lighthill 1952). Such a framework is of interest given that there is no rigorous means by which to decompose a turbulent field into acoustic and non-acoustic

† Email address for correspondence: ukarban@metu.edu.tr

components, and, therefore, no rigorous means by which to uniquely define the source of sound. Lighthill's approach—an exact rearrangement of the nonlinear Navier-Stokes system into an inhomogeneous equation comprising a linear wave operator driven by a nonlinear source term—was the first of many such reorganisations of the Navier-Stokes equations (Curle 1955; Ffowcs Williams 1963; Powell 1964; Phillips 1960; Lilley 1974; Howe 1975; Doak 1995; Goldstein 2003). All these formulations distinguish acoustic propagation from acoustic generation in a specific way, and they capture typical propagation effects like refraction in non-uniform flow with varying success.

In parallel to these developments in aeroacoustics, similar concepts were being investigated for the study of turbulence. Landahl (1967), for instance, proposed such a framework for the description of wall pressure fluctuations beneath a wall-bounded turbulent shear flow. More recently, the same underlying idea has been leveraged for the study of coherent structures in incompressible turbulent channel flow (McKeon & Sharma 2010; Hwang & Cossu 2010). The novelty of these recent studies derives from: (1) a discretisation of the inhomogeneous system; (2) a casting of the problem in frequency space; and, (3) a leveraging of the tools of linear algebra to explore the link, via the linear resolvent operator, between nonlinear interactions and the state dynamics they drive. With these three steps, the inhomogeneous system is cast in a matrix input-output form, and the relationship between 'forcing' and 'response'—in the context of aeroacoustics, 'source' and 'sound'—can be explored by considering the properties of the matrix transfer function by which they are connected: singular-value decomposition of the resolvent matrix operator can reveal the physical mechanisms by which the nonlinear forcing drives the response or by which the nonlinear source drives the acoustic field.

This framework has substantially enhanced our understanding of coherent structures in turbulent shear flow. Indeed, it provides a long-sought theoretical grounding for their definition (Towne *et al.* 2018). It has been used to study coherent structures in jets (Garnaud *et al.* 2013; Schmidt *et al.* 2018; Lesshafft *et al.* 2019; Nogueira *et al.* 2019; Pickering *et al.* 2021a) and many other flows (McKeon & Sharma 2010; Beneddine *et al.* 2016; Yeh & Taira 2019; Nogueira *et al.* 2021; Morra *et al.* 2021). In the context of jets, these coherent structures are most-often referred to as wavepackets (Crighton 1975; Jordan & Colonius 2013; Cavalieri *et al.* 2019).

The study of coherent structures has also been aided by data-processing and decomposition techniques, in particular by proper orthogonal decomposition (POD) in its numerous forms (Lumley 1970; Picard & Delville 2000; Borée 2003; Jung *et al.* 2004; Tinney *et al.* 2008; Towne *et al.* 2018). A recent study by Karban *et al.* (2022a) shows how resolvent analysis and extended spectral POD (Borée 2003) may be combined to probe turbulent shear flows in new and interesting ways. The study we report here extends this work to the jet-noise problem.

The extension is based on the fact that the resolvent framework can be tailored to choose what is considered as input (forcing) and output (response). The choice may involve a localisation in space and/or restriction to a limited number of dependent variables; for example, one may inquire as to the nature of the nonlinear interactions in a turbulent boundary layer that drive shear-stress fluctuations at the wall (Karbon *et al.* 2022a). The resolvent methodology may be similarly adapted to the jet-noise problem by restricting the forcing term to the region of vortical motion, and the response to the irrotational acoustic field (Jeun *et al.* 2016). The resolvent framework thus resembles an acoustic analogy (see the discussion in Karban *et al.* (2020)); and singular value decomposition of the acoustically tailored resolvent operator can give insight into the mechanisms by which the nonlinear flow interactions drive acoustic waves.

However, even with this rearrangement of the problem and a study of the properties of the matrix transfer function, the problem of clearly identifying the acoustically important piece of the turbulent flow remains a challenge. This is due, on one hand, to the complex,

high-rank structure of the nonlinear forcing term, and, on the other, to the formidable acoustic inefficiency of unbounded turbulence: the ratio of acoustic to turbulence fluctuation energy is of order $O(10^{-3})$ as will be shown later. These problems make it extremely difficult to craft a robust model for the acoustic source, and it is this that motivates the work we undertake. Our goal is to identify, using extensive flow data provided by large-eddy simulation, the piece of the flow that drives the acoustic field and to then propose a model for this piece of the flow that is capable of capturing effects of operating condition (jet Mach number) and forward flight.

There are many attempts in the literature to model the source of jet noise. A number of them are based on Goldstein’s generalised acoustic analogy (Goldstein 2003), where a Green’s function for the linearised Euler equations (LEE) is obtained analytically. The source terms in this configuration are defined as spatio-temporal correlations of nonlinear terms in the perturbation equations. Some source models in this framework are presented for various jet configurations in Goldstein & Leib (2008), Karabasov *et al.* (2010), Leib & Goldstein (2011), Gryazev *et al.* (2022) among others.

Another group of studies to predict jet noise are called stochastic methods, where some synthetic velocity fluctuations which satisfy two-point statistics of the flow are specified, and the acoustic field is then computed either using acoustic analogies or LEE. One branch of such stochastic approaches are called ‘stochastic noise generation and radiation’ methods, first applied to the jet noise problem by Bechara *et al.* (1994), and then modified by Billson *et al.* (2004) and Lafitte *et al.* (2011). In this method, a synthetic velocity field is obtained via summation of randomly distributed spatial Fourier modes. The energy content is defined using the von Karman-Pao energy spectrum. The resulting velocity field is convected using the mean flow, and finally, the acoustic field is predicted by applying Lighthill’s analogy on this field. Another stochastic approach used for jet-noise prediction is called the ‘random particle mesh’ (RPM) method (Siefert & Ewert 2008), where a synthetic stream function is generated by applying solenoidal filters on random signals, which then is used to compute the source terms forcing LEE to obtain pressure fluctuations.

All of the approaches discussed so far model the source correlations in the time domain. A frequency-domain model based on resolvent analysis was introduced by Towne *et al.* (2017). They provided a model function tuned using the two-point forcing correlations in the frequency domain obtained from LES data. An empirical relation using turbulent kinetic energy and dissipation rate is then provided to replace the tuning based on LES data. In another study, Pickering *et al.* (2021*b*) predicted using acoustic-field data from LES how the forcing projects onto the resolvent forcing modes. They adopted the resolvent-based estimation method given in Towne *et al.* (2020), but instead of the forcing statistics, they predicted the projection coefficients and then provided an empirical model for them. This way, they leveraged the linear mechanisms embedded in the resolvent operator associated with noise generation and model only the remaining nonlinearities coming from the forcing. Other studies have used a wavepacket source model for the near-field velocity correlations paired with Lighthill’s analogy to predict jet noise (Huerre & Crighton 1983; Cavalieri *et al.* 2011, 2012; Cavalieri & Agarwal 2014; Maia *et al.* 2019; da Silva *et al.* 2019).

In this study, we follow a strategy similar to Towne *et al.* (2017) to propose a data-driven source model that is used to predict noise generation in subsonic jets, but instead of modelling the two-point forcing correlations directly, we first isolate the acoustically efficient structures. We use the resolvent-based extended spectral proper orthogonal decomposition (RESPOD) proposed by Towne *et al.* (2015) and further developed by Karban *et al.* (2022*a*) to perform a preliminary filtering of the resolvent forcing data. This filtering extracts the forcing subspace correlated with the axisymmetric acoustic field radiated to low polar angles. The subspace so obtained contains silent-but-correlated and sound-producing components, and a second

filtering is necessary to extract the latter. The one-to-one correspondence between the SPOD modes of the acoustic field and this forcing subspace is used to show that the dominant noise generating forcing is the acoustically matched part (Ffowcs Williams 1963; Crighton 1975; Freund 2001; Cabana *et al.* 2008; Sinayoko *et al.* 2011a; Cavalieri *et al.* 2019) of the subspace. An empirical model for the sound-generating part of the field is then proposed on the basis of the acoustically matched piece of the forcing, and adapted to capture the effects of operating condition and forward flight. The advantage of the proposed strategy is that it leverages the versatility of the resolvent framework similar to Pickering *et al.* (2021b) to systematically identify the dominant noise-generation mechanisms. Different from their study, here, we start by analysing the forcing data to identify the noise-generating part and then drive the resolvent operator with this refined forcing to predict the acoustic field. Given the inefficiency of turbulence to generate noise, such an identification significantly contributes to the robustness of the final empirical model, as it retains only the essential information from the forcing data.

The paper is organised as follows: the mathematical framework for resolvent analysis and RESPOD is revisited in §2. The details about the numerical database and the resolvent-analysis tool are given in §3. The process to identify forcing components that generate downstream jet noise is explained in §4. Based on these acoustically efficient forcing components, an empirical forcing model is presented in §5, which is then adapted to include Mach-number and flight-stream effects. Concluding remarks are provided in §6.

2. Modelling framework

The resolvent framework is obtained by linearising the Navier-Stokes (N-S) equations and arranging them in input-output, or forcing-response, form in the frequency domain, where the input is nonlinear fluctuations and the output is the state. In the present case, we limit the response to be the acoustic pressure and aim to extract the forcing associated with this target response. We achieve this using resolvent-based extended spectral proper orthogonal decomposition (RESPOD) (Karban *et al.* 2022a). In this section, we briefly revisit the resolvent framework and the RESPOD approach.

2.1. Governing equations in resolvent form

The compressible N-S equations are given in compact form as

$$\partial_t \mathbf{q} = \mathcal{N}(\mathbf{q}), \quad (2.1)$$

where \mathcal{N} is the N-S operator, $\mathbf{q} = [\nu, u_x, u_r, u_\theta, p]^\top$ is the state vector, ν is specific volume and p is pressure, $\mathbf{u} = [u_x, u_r, u_\theta]^\top$ is the velocity vector in cylindrical coordinates, and x , r and θ refer, respectively, to the streamwise, radial and azimuthal directions. All variables are non-dimensionalised by the ambient speed of sound, c_∞ , the density, ρ_∞ , and the nozzle diameter, D . We consider a discretised system in space, for which linearisation around the mean, $\bar{\mathbf{q}}$, yields

$$\partial_t \mathbf{q}' - \mathbf{A} \mathbf{q}' = \mathbf{f}, \quad (2.2)$$

where $\mathbf{A} = \partial_q \mathcal{N}|_{\bar{\mathbf{q}}}$ is the linear operator obtained from the Jacobian of \mathcal{N} and \mathbf{f} contains all remaining nonlinear terms, which are referred to henceforth as the forcing terms. Equation (2.2) is Fourier transformed and rearranged to obtain

$$\hat{\mathbf{q}} = \mathbf{R} \hat{\mathbf{f}}, \quad (2.3)$$

where the hat indicates Fourier-transformed quantities and

$$\mathbf{R} = (i\omega\mathbf{I} - \mathbf{A})^{-1} \quad (2.4)$$

is the resolvent operator. The resolvent operator can be modified to limit the response to prescribed measurements via a linear transformation, \mathbf{C} , of the state vector,

$$\hat{\mathbf{y}} = \mathbf{C}\hat{\mathbf{q}}, \quad (2.5)$$

such that the input-output relation between forcing, $\hat{\mathbf{f}}$, and measurement, $\hat{\mathbf{y}}$, is given by,

$$\hat{\mathbf{y}} = \mathbf{C}\mathbf{R}\hat{\mathbf{f}}. \quad (2.6)$$

Throughout this paper, we will focus on the pressure in the acoustic field as our measured quantity; therefore \mathbf{C} is an $N_A \times 5N$ matrix, that is one in the elements that correspond to pressure in the acoustic field and zero for the rest. Here, N_A and N denote the number of discrete points in the acoustic field and the full domain, respectively.

It is also possible to impose restrictions on the forcing in (2.6) via a control matrix, \mathbf{B} , as

$$\hat{\mathbf{y}}_B = \tilde{\mathbf{R}}\hat{\mathbf{f}}, \quad (2.7)$$

where $\tilde{\mathbf{R}} \triangleq \mathbf{C}\mathbf{R}\mathbf{B}$ denotes the modified resolvent operator. Note that, $\hat{\mathbf{y}}_B \neq \hat{\mathbf{y}}$ in general. \mathbf{B} will later be used to identify irrelevant forcing components for the jet-noise problem: i.e. those terms which, when suppressed by \mathbf{B} , do not lead to changes in the measurement, such that $\hat{\mathbf{y}}_B = \hat{\mathbf{y}}$.

2.2. Resolvent-based extended spectral proper orthogonal decomposition

One of the goals of this study, and indeed one of the broader goals of jet-noise modelling, is to obtain simplified representations or models of the nonlinear interactions that underpin jet noise. One such approach is to search for a useful rank reduction. A known trait of turbulent jets and their sound is the marked difference in complexity between the turbulence and acoustic fields. This difference implies that, given a discretised turbulent jet database, it may be possible to represent the acoustic field using a compact basis with a small number of vectors, yielding a low-rank system, while a substantially larger basis will be required to define the turbulent fluctuations, and thus the forcing, in the near field, yielding a high-rank system. A central idea underlying the approach we follow here is as follows: given the linear relation between the forcing and the target response in (2.6), the low-rank structure of the acoustic field suggests the existence of a low-rank, acoustically active forcing subspace. It is necessary to identify this subspace, because it is there that modelling work can be done.

There exist several ways to identify the forcing associated with a given response. A detailed analysis was provided in Karban *et al.* (2022a), where a method referred to as ‘Resolvent-based Extended Spectral Proper Orthogonal Decomposition’ (RESPOD) was used to achieve the abovementioned identification. RESPOD is based on the extended proper orthogonal decomposition presented by Borée (2003) and is related to spectral proper orthogonal decomposition (SPOD) (Lumley 1970; Picard & Delville 2000; Towne *et al.* 2018). The aim in RESPOD is to find a forcing mode, $\chi^{(p)}$, that is correlated with the p^{th} SPOD mode, $\psi^{(p)}$, of the measured response, $\hat{\mathbf{y}}$. It was first presented in Towne *et al.* (2015) and later discussed in Karban *et al.* (2022a) to identify the forcing structures that generate wall-attached eddies. Here, we briefly review the method highlighting how it can be adapted to find the low-rank forcing subspace associated with sound generation.

For a given ensemble of realizations $\hat{\mathbf{Y}} = [\hat{\mathbf{y}}_1 \cdots \hat{\mathbf{y}}_P]$ of an N dimensional discretised system, where P is the number of Fourier realizations, SPOD involves eigen-decomposition

of the CSD matrix $\hat{\mathbf{S}} \triangleq \hat{\mathbf{Y}}\hat{\mathbf{Y}}^H$,

$$\hat{\mathbf{S}} = \hat{\Psi}\hat{\Lambda}\hat{\Psi}^H, \quad (2.8)$$

where the eigenvectors, $\hat{\Psi}$, and eigenvalues, $\hat{\Lambda}$, of $\hat{\mathbf{S}}$ are the SPOD modes and gains, respectively. An alternative way to obtain the SPOD modes, as shown in Towne *et al.* (2018), is to perform the eigendecomposition

$$\hat{\mathbf{Y}}^H \mathbf{W} \hat{\mathbf{Y}} = \hat{\Theta}\hat{\Lambda}\hat{\Theta}^H, \quad (2.9)$$

where \mathbf{W} is a positive-definite weight matrix, and $\hat{\Theta}$ is a matrix containing the eigenmodes of $\hat{\mathbf{Y}}^H \mathbf{W} \hat{\mathbf{Y}}$. The eigenmodes, $\hat{\Psi}$ and $\hat{\Theta}$, are related as

$$\hat{\Psi} = \hat{\mathbf{Y}}\hat{\Theta}\hat{\Lambda}^{-1/2}, \quad (2.10)$$

or alternatively as

$$\hat{\Theta} = \hat{\mathbf{Y}}^H \mathbf{W} \hat{\Psi} \hat{\Lambda}^{-1/2}. \quad (2.11)$$

Equation (2.10) indicates that it is possible to obtain the SPOD modes as a linear combination of the realizations. Writing (2.7) with $\mathbf{B} = \mathbf{I}$ for the ensemble of realizations as

$$\hat{\mathbf{Y}} = \tilde{\mathbf{R}}\hat{\mathbf{F}}, \quad (2.12)$$

where $\hat{\mathbf{F}} \triangleq [\hat{f}_1 \cdots \hat{f}_P]$ is the matrix of the forcing realisations, and multiplying (2.12) by $\hat{\Theta}\hat{\Lambda}^{-1/2}$ yields

$$\hat{\Psi} = \tilde{\mathbf{R}}\hat{\mathbf{F}}\hat{\Theta}\hat{\Lambda}^{-1/2}. \quad (2.13)$$

Equation (2.13) can be written for the p^{th} SPOD mode by extracting the corresponding columns in the matrices, $\hat{\Psi}$, $\hat{\Theta}$ and $\hat{\Lambda}$,

$$\hat{\psi}^{(p)} = \tilde{\mathbf{R}}\hat{\mathbf{F}}\hat{\theta}^{(p)}\lambda^{(p)-1/2}, \quad (2.14)$$

where $\hat{\theta}^{(p)}$ denotes the p^{th} column in $\hat{\Theta}$ and $\lambda^{(p)}$ denotes the p^{th} diagonal element in $\hat{\Lambda}$. We then define the RESPOD mode of the forcing, $\hat{\chi}^{(p)}$, as

$$\hat{\chi}^{(p)} \triangleq \hat{\mathbf{F}}\hat{\theta}^{(p)}\lambda^{(p)-1/2}. \quad (2.15)$$

Following Borée (2003), it can be shown that the RESPOD mode, $\chi^{(p)}$, contains all the forcing components correlated with the SPOD mode, $\psi^{(p)}$. Furthermore, (2.14) indicates that the two modes are connected via the resolvent operator as

$$\hat{\psi}^{(p)} = \tilde{\mathbf{R}}\hat{\chi}^{(p)}. \quad (2.16)$$

The ability to identify a RESPOD mode of the forcing with each SPOD mode of the response implies, for the jet-noise problem, that one can use this approach to identify the low-rank forcing subspace that is correlated with the low-rank acoustic field, and which, furthermore, generates the low-rank acoustic field when applied to the resolvent operator.

We will use this approach to obtain a low-rank representation of the forcing that is responsible for most of the acoustic energy radiated by a turbulent jet. The advantage of identifying a low-rank forcing is twofold: (i) one needs to model only that piece in the forcing; (ii) not dealing with the entire CSD matrix of the forcing is convenient in terms of computing the response, which would otherwise require multiplication of the resolvent operator by an $N \times N$ matrix, where N is generally very large. Given the number of realisations,

P , and the degree of freedom, N , which usually satisfy $P \ll N$, this approach provides a computationally inexpensive means of obtaining a low-rank system.

3. Numerical databases and tools

The numerical analysis in this study is conducted in two stages: (i) identification of low-rank forcing by post-processing a large eddy simulation (LES) database, and (ii) performing acoustic predictions by computing the response of the resolvent operator driven by the identified forcing modes. In the following subsections, we provide details about the LES database and the resolvent analysis, respectively.

3.1. Large eddy simulation database

The numerical database used in this study to develop an empirical forcing model consists of LES of four subsonic jets, one at jet Mach number, $M_j \triangleq U_j/c_j = 0.4$, with no flight effect and others at $M_j = 0.9$ with or without flight effect. We use three other LES databases at $M_j = 0.7$ with or without flight effect and at $M_j = 0.8$ without flight effect to test the model. The LES was conducted using the unstructured flow solver ‘Charles’ (Brès *et al.* 2017). In all cases, the jets are isothermal and ideally expanded. Two of the cases at $M_j = 0.9$ contain a flight stream at $M_\infty = 0.15$ and 0.3 , respectively. All jets are turbulent thanks to a synthetic forcing applied inside nozzle. Other parameters related to each simulation are tabulated in Table 1, where $Re = \rho_j U_j D / \mu_j$ denotes the Reynolds number, μ denotes the dynamic viscosity, D is nozzle diameter, U , P and T denote the mean streamwise velocity, pressure and temperature, respectively, c.v. stands for control volume, $dt = \tilde{d}t c_\infty / D$ and $t_{\text{sim}} = \tilde{t}_{\text{sim}} c_\infty / D$ are time step and total time of the simulation in acoustic units, where \tilde{t} is the physical time, and Δt is the time step in acoustic units used for data storage. The subscripts, j , ∞ and 0 denote jet exit, free-stream and stagnation conditions, respectively. Throughout this paper, velocities are non-dimensionalized with the ambient speed of sound, c_∞ , lengths with nozzle diameter, D , pressure with $\rho_\infty c_\infty^2 / 2$, and time with c_∞ / D . Frequencies are reported in Strouhal number, $St = \tilde{f} D / U_j$, where f is the dimensional frequency.

The axisymmetric nature of jets renders possible decomposing the flow into azimuthal Fourier modes and analysing them separately. To facilitate azimuthal Fourier decomposition, for each case, the LES data is interpolated onto a cylindrical grid with mesh size $(N_x, N_r, N_\theta) = (656, 138, 128)$, where N_x , N_r and N_θ are the number of grid points in streamwise, radial and azimuthal directions. The cylindrical grid extends in $x, r, \theta \in [0, 30] \times [0, 6] \times [0, 2\pi]$.

The linearised N-S equations in the time domain for the m^{th} azimuthal Fourier mode are given as

$$\partial_t \mathbf{q}'^{(m)} - \mathbf{A}^{(m)} \mathbf{q}'^{(m)} = \mathbf{f}^{(m)}, \quad (3.1)$$

where the superscript (\cdot) denotes the azimuthal mode number. We limit our analysis to the acoustic field in the first azimuthal mode, $m = 0$, only.

In figure 1, snapshots of pressure and temperature for the first azimuthal Fourier mode, $m = 0$, are shown for the four cases used for tuning of the empirical model. Temperature is shown as an indicator of turbulent fluctuations in the shear layer. Pressure is saturated to show the acoustic waves propagating from the jets. It is seen that the case M09Mc00 (see table 1 for case abbreviations) has the strongest pressure gradients, and thus, highest noise level. Existence of the flight stream suppresses both the turbulent fluctuations and the noise generated by the jet, at a level increasing with the flight velocity. The flow fields for the remaining three cases are not shown for brevity. All seven cases are validated against

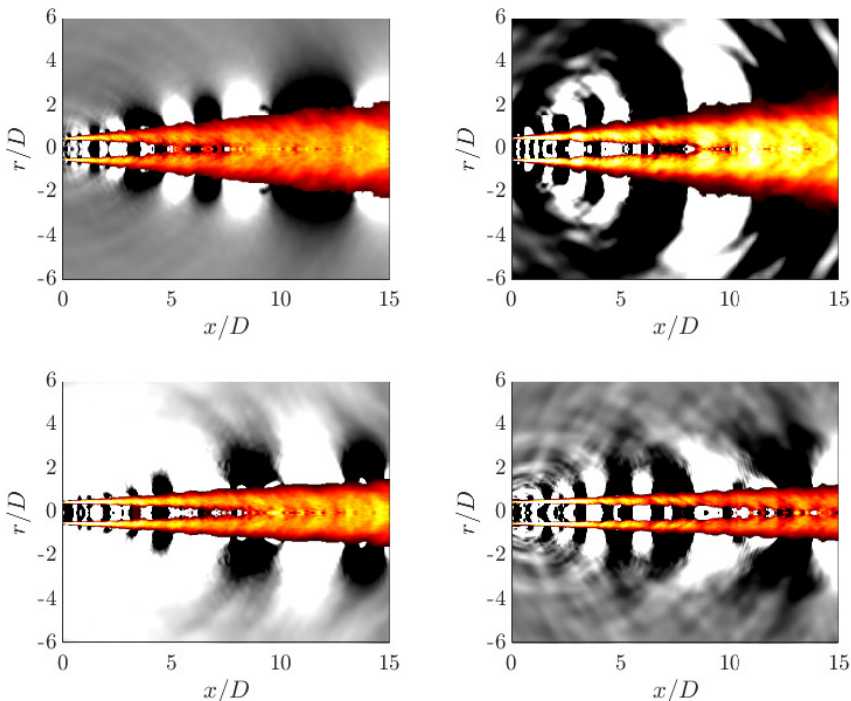


Figure 1: Snapshots of the first azimuthal Fourier mode of pressure (grey) and temperature (color) for the cases M04Mc00 (top-left), M09Mc00 (top-right), M09Mc15 (bottom-left), M09Mc30 (bottom-right). Color-scale for pressure linearly varies between $[-6 \times 10^{-3}, 6 \times 10^{-3}]$ for all cases. Color-scale for temperature is given as $[1, 1.01]$, $[1, 1.03]$, $[1, 1.02]$, $[1, 1.02]$ for the abovementioned four cases, respectively.

Table 1: Details of the LES database. The first four and the last three cases are used to tune and test the empirical model, respectively.

case	Re	M_j	M_∞	P_0/P_∞	T_0/T_∞	# of c.v.	dt	Δt	t_{sim}
M04Mc00	0.45×10^6	0.4	0.0	1.12	1.03	16×10^6	1×10^{-3}	0.1	3000
M09Mc00	1.01×10^6	0.9	0.0	1.69	1.16	16×10^6	1×10^{-3}	0.1	2000
M09Mc15	1.01×10^6	0.9	0.15	1.69	1.16	22×10^6	1×10^{-3}	0.1	2000
M09Mc30	1.01×10^6	0.9	0.3	1.69	1.16	22×10^6	1×10^{-3}	0.1	2000
M07Mc00	0.79×10^6	0.7	0.0	1.39	1.10	22×10^6	1×10^{-3}	0.1	2000
M07Mc15	0.79×10^6	0.7	0.0	1.39	1.10	22×10^6	1×10^{-3}	0.1	2000
M08Mc00	0.90×10^6	0.8	0.15	1.52	1.13	22×10^6	1×10^{-3}	0.1	2000

experimental data. A detailed validation can be found in Brès *et al.* (2018) for the cases M04Mc00 and M09Mc00 and in Maia *et al.* (2022) for the remaining cases. The M09Mc00 case is publicly available as part of a database for reduced-complexity modelling of fluid flows (Towne *et al.* 2022).

The case M04Mc00 contains both the state and the forcing data while others contain only the state data. The forcing data, once the state data is stored, is obtained via the procedure devised in Towne (2016) and summarised in algorithm 1. Both the state and forcing data

Algorithm 1 Computing the forcing

- 1: Calculate the state \mathbf{q} through LES with $dt = 0.001$ and store it at every 200th time step.
 - 2: Calculate and save the mean flow $\bar{\mathbf{q}}$.
 - 3: Calculate and save $\mathcal{G}(\bar{\mathbf{q}})$, where \mathcal{G} is the nonlinear LES operator. Note that \mathcal{G} is different from the N-S operator, \mathcal{N} , as the sub-grid scales are filtered in \mathcal{G} .
 - 4: For each snapshot, calculate $\partial\mathbf{q}/\partial t = \mathcal{G}(\mathbf{q})$.
 - 5: For each snapshot, calculate $\mathbf{A}\mathbf{q}' \approx \frac{\mathcal{G}(\bar{\mathbf{q}} + \epsilon\mathbf{q}') - \mathcal{G}(\bar{\mathbf{q}})}{\epsilon}$, where ϵ is a sufficiently small number.
 - 6: Interpolate \mathbf{q} , $\partial\mathbf{q}/\partial t$, and $\mathbf{A}\mathbf{q}'$ data onto the cylindrical grid.
 - 7: Compute the forcing in the time domain using (2.2).
-

are Fourier transformed using blocks containing 512 snapshots in time with an overlap ratio of 75%. To minimize spectral leakage, we use an exponential windowing function (Martini *et al.* 2019),

$$W(t) = e^{n\left(4 - \frac{T}{t(T-t)}\right)}, \quad (3.2)$$

with $n = 1$ and window size $T = 512\Delta t$. The correction discussed in Martini *et al.* (2019), which is necessary to satisfy (2.3) when a windowing function is applied during the temporal Fourier transform (FT), is implemented while computing the forcing terms in the frequency domain. The correction is shown in Nogueira *et al.* (2021) to significantly improve the convergence of resolvent-based prediction of the response via (2.3).

3.2. Resolvent analysis

Resolvent-based prediction of the response using the forcing data is achieved via a custom resolvent analysis code (Bugeat *et al.* 2019). The code uses the finite-volume method to solve the linearised N-S equations decomposed into azimuthal Fourier modes. The input-output relation in (2.3) is written for a given azimuthal mode, m , as

$$\hat{\mathbf{q}}^{(m)} = \mathbf{R}^{(m)} \hat{\mathbf{f}}^{(m)}, \quad (3.3)$$

where $\mathbf{R}^{(m)} \triangleq (i\omega\mathbf{I} - \mathbf{A}^{(m)})^{-1}$. In practice, the response, $\hat{\mathbf{q}}^{(m)}$, to a given forcing $\hat{\mathbf{f}}^{(m)}$ is computed by solving the linear system

$$\mathbf{L}^{(m)} \hat{\mathbf{q}}^{(m)} = \hat{\mathbf{f}}^{(m)}, \quad (3.4)$$

where $\mathbf{L}^{(m)} = \mathbf{R}^{(m)-1} = (i\omega\mathbf{I} - \mathbf{A}^{(m)})$ is a sparse linear operator. The resolvent code solves (3.4) via LU decomposition using the PETSc library (Balay *et al.* 1997). Further details can be found in Bugeat *et al.* (2019).

The original code was written based on conservative variables, while the LES forcing database was generated using the primitive-like variable set, $\mathbf{q} = [\nu, \mathbf{u}, p]$, as discussed in §2.1, yielding a compatibility issue. To overcome this issue, a correction derived by Karban *et al.* (2020) is implemented.

The sound level in the acoustic field is predicted by first computing the response to individual forcing realisations (or, instead, the RESPOD modes of the forcing) solving (3.4) and then calculating the power spectral densities (PSD) based on these individual response realisations (or modes, instead).

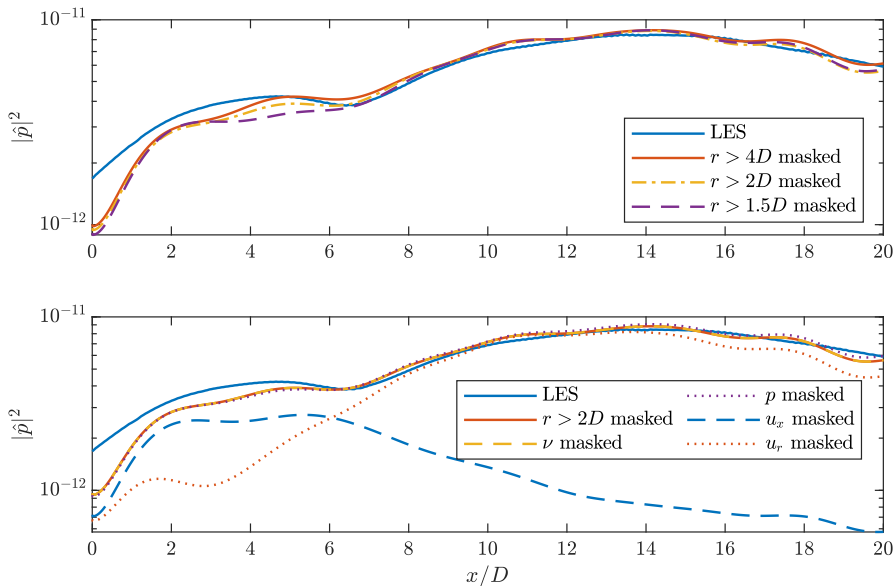


Figure 2: PSD of pressure predicted using resolvent analysis with masking applied in space (top) and in variables (bottom) in comparison to the LES data at $r = 5D$ for the case M04Mc00 at $St = 0.6$.

4. Identification of the acoustically efficient forcing components

The goal of this study is to extract acoustically relevant forcing components that underpin noise-generation mechanisms in subsonic jets and to propose an empirical model for these components. Identification of the noise-generating part of the forcing prior to empirical modelling is crucial for the model to yield robust acoustic predictions. To achieve this, we proceed as follows. Using the database M04Mc00, which contains both the state, \mathbf{q} , and the forcing, \mathbf{f} , we first conduct the analysis outlined in §2 based on RESPOD to identify the acoustically active forcing components. We limit the study to mechanisms associated with noise generation at low polar angles, which we refer to as downstream noise. We then discuss how to further decompose the low-rank forcing associated with the acoustic field to extract the part which satisfies the acoustic matching criterion (Ffowcs Williams 1963; Crighton 1975).

4.1. Masking the forcing vector

Before performing a dedicated analysis to obtain a low-rank forcing model, we first reduce the number of the forcing terms to model. This is achieved by applying spatial and componentwise masking in the forcing data to observe the effect of the masked regions/components on noise generation. This masking involves zeroing certain parts of the forcing vector using the matrix \mathbf{B} . Figure 2 shows the result of different masks in terms of the PSD of the acoustic pressure at $St = 0.6$. Masking the forcing beyond $r > 2D$ or $r > 4D$ yields nearly identical results in the entire flow domain. Masking beyond $r > 1.5D$ also yields nearly identical noise fields in the downstream region, $x > 6D$, while a slight discrepancy is observed in the region $x/D \in [3, 6]$. We therefore consider the forcing in the region $r < 2D$ for the rest of the analysis.

Componentwise masking of the forcing shows that the components f_ν and f_p , which

correspond to the mass and energy equations, respectively, have negligible contribution to the acoustic field. Masking the component f_{u_r} , which is the forcing associated with the radial momentum equation, causes significant reduction in the sideline noise while not affecting the acoustic field in the downstream region. On the other hand, masking the component f_{u_x} , which is the forcing associated with the streamwise momentum, causes significant reduction in the downstream noise while having limited effect on the sideline noise. These results indicate that the forcing term f_{u_x} in the region $r < 2D$ is solely responsible for downstream noise generation, consistent with the observation of Freund (2001) using Lighthill's analogy. In what follows, focusing on the downstream noise generation only, we aim to identify the acoustically active subspace associated with this single forcing component.

4.2. Applying RESPOD to obtain low-rank forcing

We now aim to obtain a low-rank representation of the subspace of the forcing associated with the most-energetic components of the acoustic field. To achieve this, we first compute the SPOD modes of the acoustic field, and we then use RESPOD to extract the associated forcing modes, as described in §2.2. In figure 3, the SPOD eigenvalues of the pressure in the downstream acoustic field, defined as $x/D, r/D \in [6, 30] \times [4, 6]$, and those of the forcing term f_{u_x} in the turbulent region, defined as $x/D, r/D \in [0, 30] \times [0, 2]$, are shown for $St = 0.6$. For the acoustic field, the leading SPOD eigenvalue corresponds to more than 75% of the total acoustic energy. The sum of the first five SPOD eigenvalues corresponds to 99% of the total acoustic energy, indicating a low-rank organisation in the acoustic field. For the forcing in the near field, on the other hand, the leading SPOD mode contains less than 6% of the total energy in f_{u_x} . Around one hundred modes are required to capture 90% of the total forcing energy, indicating an extremely high-rank structure. As discussed earlier, this difference between the near-field turbulence forcing and the acoustic field is the crux of the jet-noise problem, which we aim to overcome by educing the small portion of the forcing responsible for the acoustic field.

Using RESPOD, we extract from this high-rank forcing data a low-rank subspace that is correlated with the low-rank pressure structures observed in the acoustic field. In figure 4, we show the leading SPOD mode of pressure in the acoustic field and the associated RESPOD mode of the forcing in the near field, together with the energy distribution of the first twenty RESPOD forcing modes. The leading SPOD mode takes the form of an acoustic wave propagating at some angle, while the associated RESPOD forcing mode contains a disorganised structure, which may imply underconvergence in the forcing mode, despite the very long time-series used for the analysis. The first RESPOD mode contains less than 0.8% of the total forcing energy, but it is associated with the leading SPOD mode of the acoustic field, corresponding to 75% of the total noise in the downstream region. This result shows the importance of applying such an identification prior to any modelling effort. Without this extraction of the low-rank forcing structure, a fitting function optimised using the forcing data will be affected by the existence of energetic structures that do not significantly contribute to sound generation.

No smooth trend is observed in the energy of the first twenty RESPOD forcing modes, contrary the SPOD modes in the acoustic field. As discussed in Karban *et al.* (2022a), RESPOD does not impose a strict filtering on the forcing to extract the *active* structures that actually drive the acoustic field, but finds the correlated part which includes silent-but-correlated structures. Lack of a smooth trend in the energy of the RESPOD forcing modes implies underconvergence of these modes. Given that the active part in the RESPOD forcing modes are linearly related to the SPOD modes of the acoustic field, they should experience the same convergence rate. The underconvergence in the RESPOD forcing modes can then be attributed to the contribution of the silent-but-correlated structures, causing

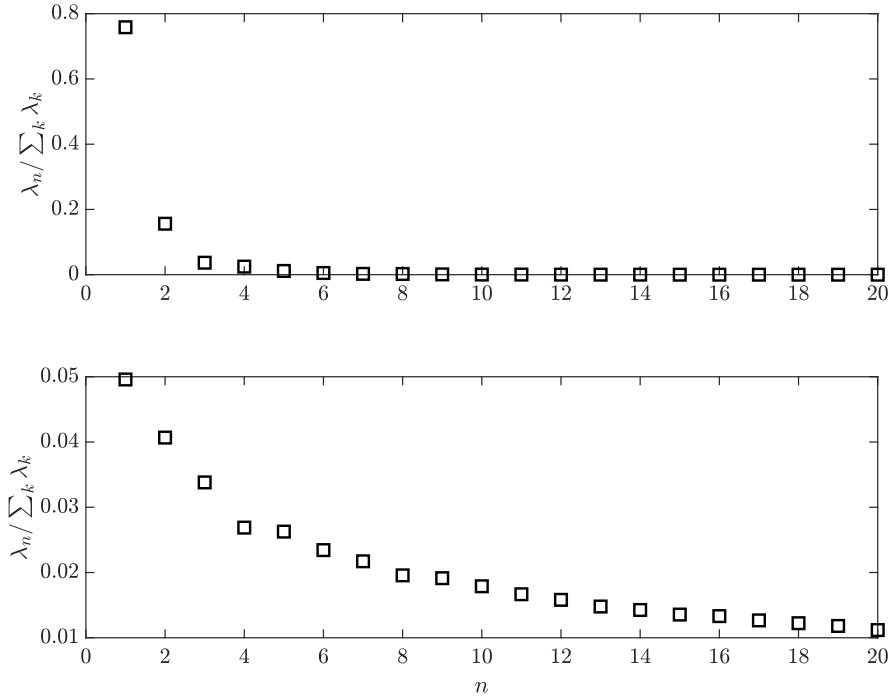


Figure 3: SPOD eigenvalues of the pressure in the acoustic field (top) and streamwise forcing, f_{u_x} , in the near field (bottom) for the case M04Mc00 at $St = 0.6$.

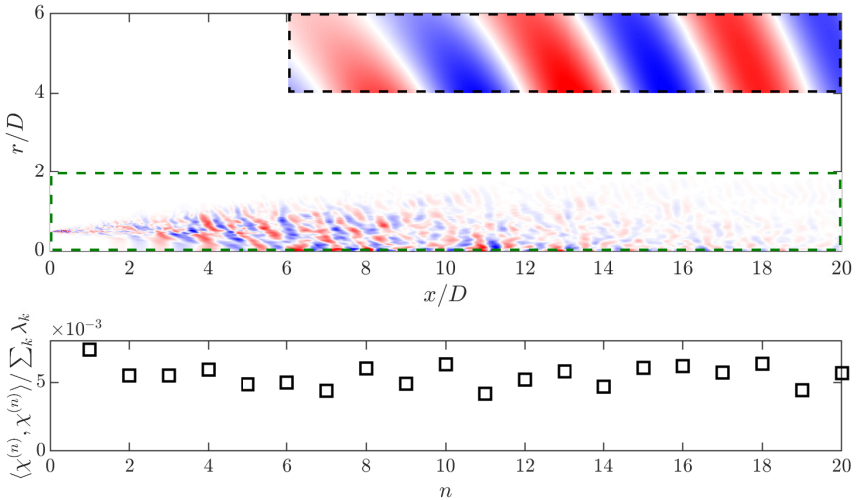


Figure 4: Optimal SPOD mode of acoustic pressure and the associated RESPOD mode of the forcing (top) together with the energy distribution in the first twenty RESPOD modes of the forcing (bottom) for the case M04Mc00 at $St = 0.6$. The acoustic and forcing fields in the top plot are denoted by the black and green dashed boxes, respectively.

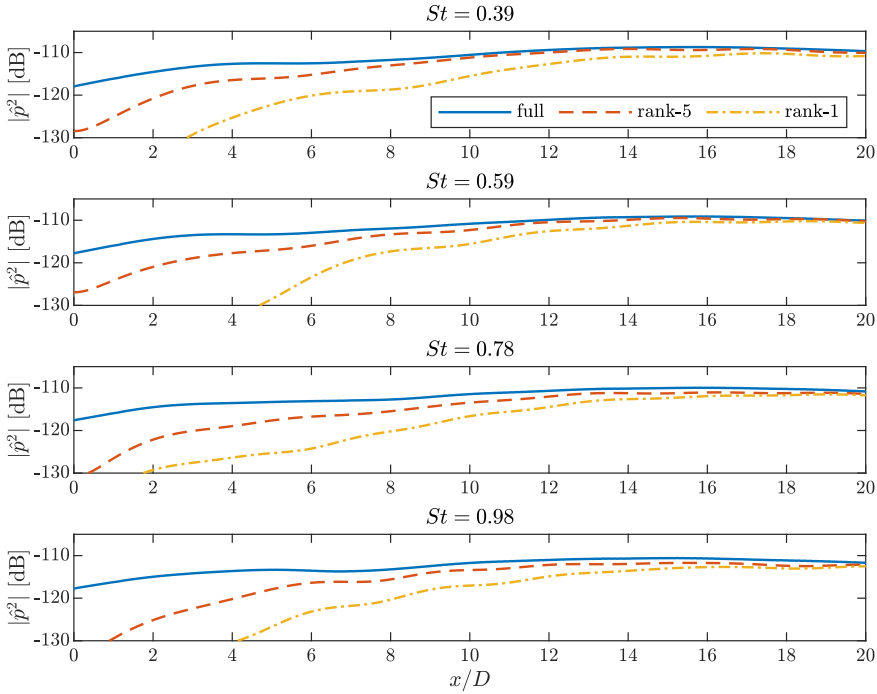


Figure 5: PSD of acoustic pressure generated using rank-5 and rank-1 forcing, respectively, obtained by RESPOD, in comparison to the acoustic field obtained from LES data (corresponding to full-rank forcing in the ideal case) at different frequencies ranging from $St = 0.4$ to 1 (from top to bottom).

also the mode shape to be significantly less organised compared to the associated SPOD mode. This underconvergence observed in the forcing modes does not pose a problem in the following analysis. The SPOD modes of the response and the RESPOD modes of the forcing are computed using Fourier realisations of response and forcing that exactly correspond to the same time window. In the ideal case of an error-free database, (2.3) is therefore satisfied for each pair of response-forcing realisations. So, no matter how underconverged the forcing data is, the structures generating the converged acoustic field are, by construction, ensured to be contained in the forcing mode seen in figure 4.

As discussed in §2.2, the first RESPOD forcing mode contains all structures correlated with the leading SPOD mode. This indicates that the remaining forcing that amounts to 99% of the total forcing energy can generate only 25% of the total acoustic energy. In figure 5, we show a comparison of the true acoustic field and the acoustic fields obtained using rank-5 and rank-1 forcing truncations obtained using RESPOD for a number of frequencies, $St \in [0.4, 1]$. The rank-5 forcing recovers nearly the entire acoustic field in the downstream region. The rank-1 forcing also recovers a significant portion of the downstream acoustic field. Although the acoustic field predicted by the rank-1 forcing should correspond to 75% of the total acoustic energy, the actual prediction amounts to less than this ratio. This is due to the errors contained in the LES database, causing a loss in the correlation information between the response and the forcing. Despite all the limitations of the existing database as discussed in appendix A, we see that it is still possible to define a rank-1 forcing which can generate most of the downstream noise.

In what follows, we further decompose the rank-1 forcing obtained by RESPOD to extract

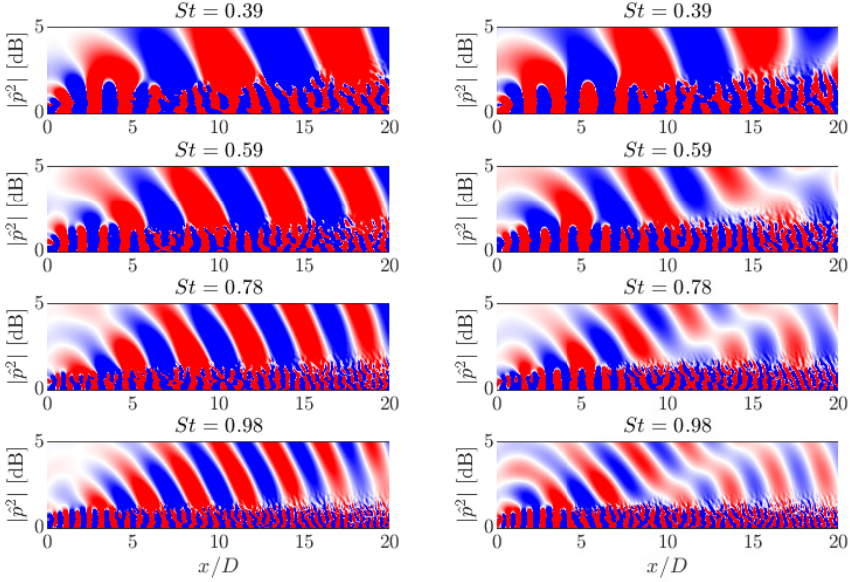


Figure 6: Real part of the pressure generated using first (left), and second (right) RESPOD mode of the forcing at different frequencies ranging from $St = 0.4$ to 1 (from top to bottom). Color scale ranges between $[-1 \times 10^{-6}, 1 \times 10^{-6}]$.

the acoustically active forcing components which drive the leading SPOD mode of the acoustic pressure seen in figure 4.

4.3. Isolating the radiating component of the low-rank forcing

In figure 6, the acoustic fields generated by the first two RESPOD modes are shown for the case M04Mc00 at a number of frequencies, $St \in [0.4, 1.0]$. The first modes at all frequencies contain a single wave propagating at some angle with no jump in the phase. On the other hand, there exists a phase shift in the second modes that moves upstream with increasing frequency. The phase shift appears in order to satisfy orthogonality between the first and the second modes, which is expected as RESPOD finds the forcing modes that generate the SPOD modes, which comprise an orthogonal basis. Note, however, that, no such orthogonality is ensured for the forcing modes.

Looking at the acoustic field of the first RESPOD mode, it is apparent that the propagation angle is nearly constant, around 30° when measured from the downstream end, for all frequencies, reminiscent of a Mach-wave-like mechanism (c.f. Tam *et al.* (2008)). To explore this trend, we consider a wave in the streamwise direction defined by, $\exp(-ik_x x)$, where k_x is the streamwise wavenumber associated with a phase speed

$$c_x = \omega/k_x, \quad (4.1)$$

where $\omega = 2\pi St$ is the angular frequency. For a Mach-wave-like mechanism, the phase speed is greater than the speed of sound, c_∞ , and the propagation angle is given by $\cos^{-1}(c_\infty/c_x)$ (Ffowcs Williams 1963; Crighton 1975). We project the first and the second RESPOD forcing modes onto this wave, varying in the phase speed over the range $[c_\infty, 2c_\infty]$, yielding

$$a^{(p)}(k_x, St) = \langle \chi^{(p)}(x, r, St), e^{-ik_x x} \rangle \triangleq \int_S \chi^{(p)}(x, r, St) e^{-ik_x x} dS, \quad (4.2)$$

where p is the RESPOD mode number and S is the 2D domain spanning the x and r directions.

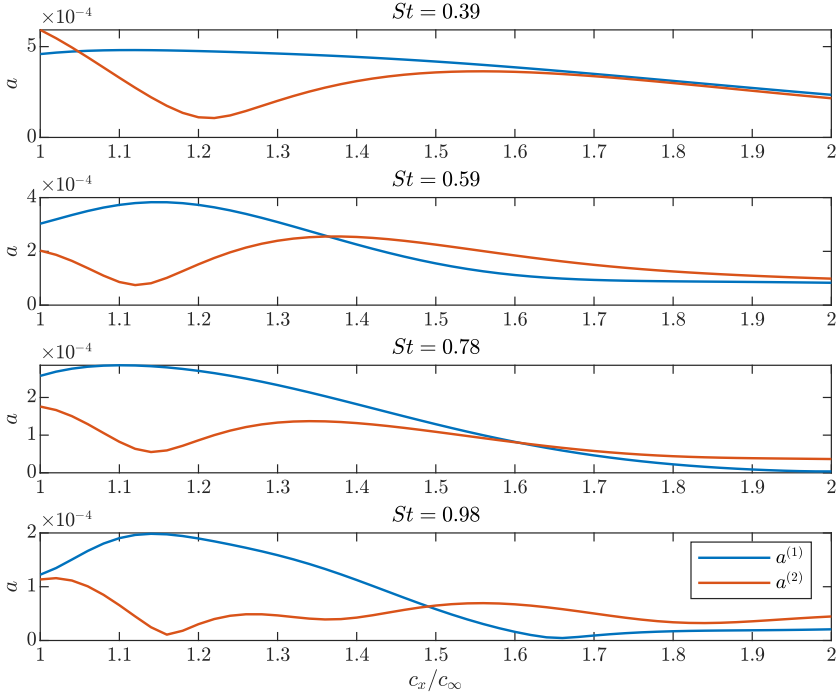


Figure 7: Projection of first and second RESPOD modes of the forcing, respectively, onto streamwise harmonic waves with supersonic phase speeds. Different frequencies ranging from $St = 0.4$ to 1 are shown from top to bottom.

The results are shown in figure 7. It is seen that at all frequencies, the projection coefficient, $a^{(1)}$, peaks around $1.1-1.2c_\infty$, which corresponds to an angle of $\sim 30^\circ$, consistent with the propagation angle observed in the acoustic response field. The coefficient, $a^{(2)}$, on the other hand, has a dip around the same value at all frequencies, reminiscent of the orthogonality observed in the response modes of figure 6.

These results suggest that projection of the forcing onto supersonic waves is the relevant mechanism for generation of downstream noise, consistent with previous hypotheses and models (Freund 2001; Cavalieri *et al.* 2012; Jordan & Colonius 2013; Cavalieri *et al.* 2019). To test this hypothesis, we define the following Fourier transform (FT) in the streamwise direction,

$$\mathcal{F}_x(\mathbf{a}) = \int_0^L \mathbf{a} e^{-ik_x x} dx, \quad (4.3)$$

where $L = 30D$ is the domain length. Using this FT, we decompose the first RESPOD mode of the forcing, $\chi^{(1)}$, into two parts, $\chi^{(1-)}$ and $\chi^{(1+)}$, containing subsonic and supersonic components, respectively (Sinayoko *et al.* 2011*b*). The resulting forcing fields are depicted in comparison to the original forcing mode in figure 8. It is seen that most of the forcing energy is contained in the subsonic part of the mode, $\chi^{(1-)}$, making it indistinguishable from $\chi^{(1)}$. The supersonic component, $\chi^{(1+)}$, takes the form of a compilation of radially thin wavepackets with a disorganised radial phase structure.

The acoustic response generated by these subsonic and supersonic modes, $\chi^{(1-)}$ and $\chi^{(1+)}$, respectively, are compared to the response of the entire first RESPOD mode of the forcing,

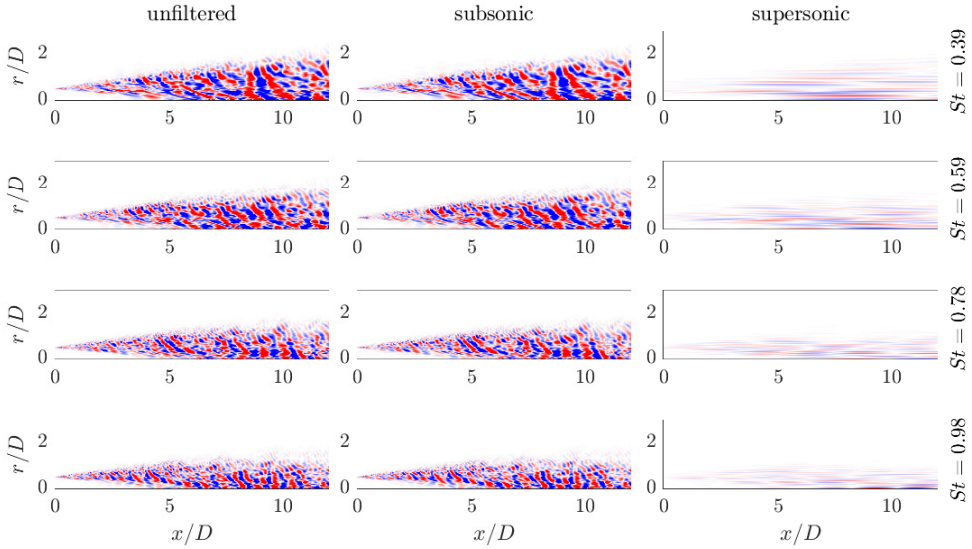


Figure 8: Real part of the first RESPOD mode of the forcing (left) compared to its subsonic (middle) and supersonic (right) parts. Different frequencies ranging from $St = 0.4$ to 1 are shown from top to bottom.

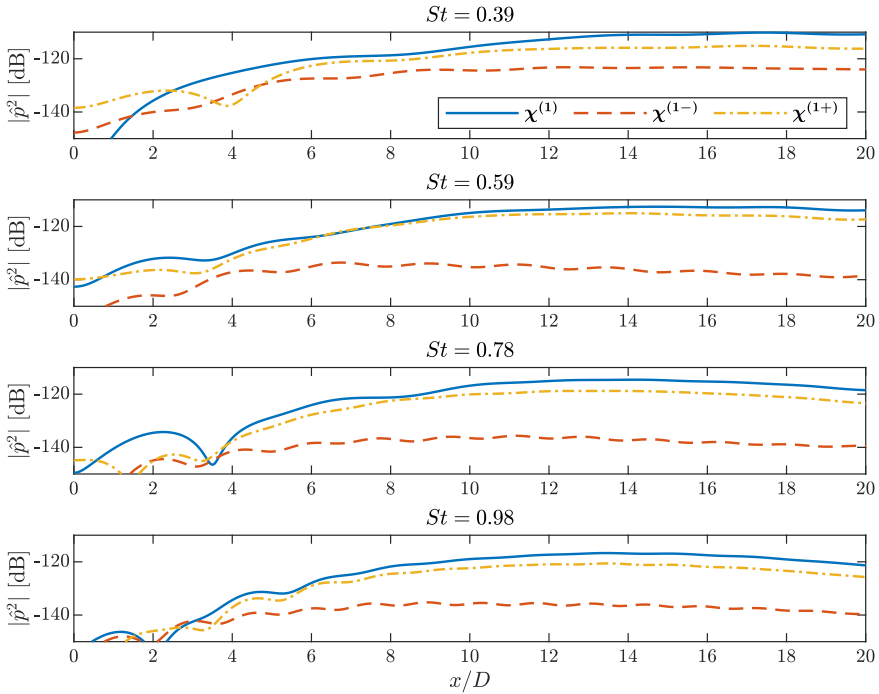


Figure 9: PSD of the acoustic pressure generated by the first RESPOD mode of the forcing (solid) compared to its subsonic (dashed) and supersonic (dash-dotted) parts. Different frequencies ranging from $St = 0.4$ to 1 are shown from top to bottom.

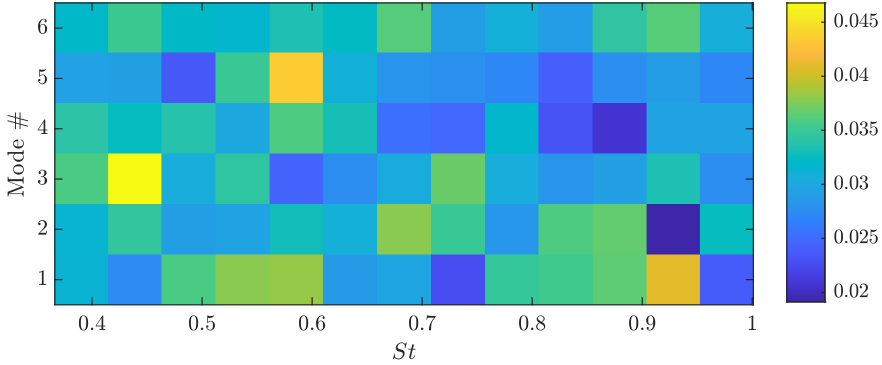


Figure 10: Energy ratio of the supersonic part of the RESPOD mode of the forcing.

$\chi^{(1)}$, in figure 9 for a range of frequencies. It is clear that the supersonic modes underpin noise generation at all frequencies. Removing the supersonic components leads to more than an order-of-magnitude reduction in sound generation. The energy contained in the supersonic part of the RESPOD modes of the forcing is shown in figure 10 for different mode numbers and frequencies. For all the modes and frequencies, the supersonic components contain less than 5% of the mode energy. The first RESPOD mode of the forcing already contains less than 1% of the total forcing energy, which means that the energy fraction of the supersonic part of the first RESPOD mode of the forcing, $\chi^{(1+)}$, with respect to the total forcing energy at the same frequency, is $\sim 0.04\%$, while it generates $\sim 75\%$ of the total acoustic energy in the downstream region for a frequency range $St = [0.4, 1.0]$ at $M_j = 0.4$.

5. Empirical modelling of the acoustically efficient forcing component

Having identified the acoustically efficient forcing components, we now characterise these modes and propose an empirical forcing model. In what follows, we first present a modelling strategy based on the supersonic part of the first RESPOD mode of the forcing for the case M04Mc00, which yields a fundamental form of the model equation. The model parameters are chosen such that they can be easily adapted to account for frequency, jet Mach number and flight effect. We then use the acoustic fields obtained from the LES to tune the parameters. Given the high energy contained in the optimal SPOD mode of the acoustic pressure in the downstream region, we focus on modelling the supersonic part of the first RESPOD mode of the forcing only; i.e., we construct a rank-1 model.

5.1. Empirical source modelling for $M_j = 0.4$

As shown in figure 8, the supersonic mode, $\chi^{(1+)}$, roughly follows the jet spreading and has the form of thin wavepackets elongated in the streamwise direction spanning most of the flow domain. Given the radial randomness of these thin wavepackets, a model for the x - r structure is not feasible. We therefore make use of the characteristics of the modified resolvent operator, $\tilde{\mathbf{R}}$, which yields the acoustic pressure as the response thanks to the measurement matrix \mathbf{C} .

In resolvent analysis, a singular value decomposition (SVD) of the resolvent operator is used to identify mechanisms by which the output (acoustic pressure in our case) is driven by the input (forcing). The SVD is given as

$$\tilde{\mathbf{R}} = \mathbf{U}\mathbf{\Sigma}\mathbf{V}^H, \quad (5.1)$$

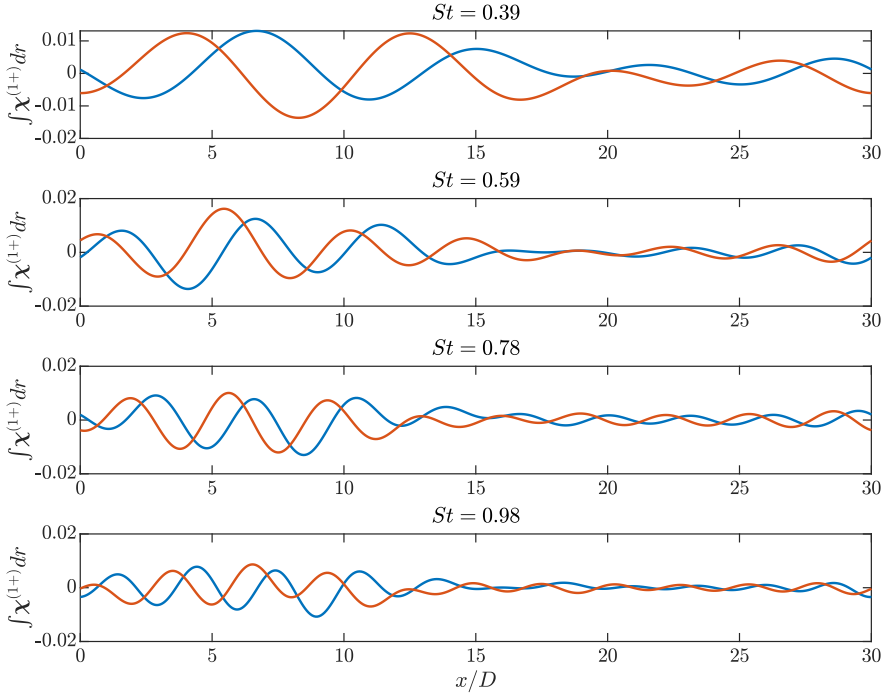


Figure 11: Real (blue) and imaginary (orange) parts of the supersonic part of the first RESPOD mode of the forcing integrated in the radial direction. Different frequencies ranging from $St = 0.4$ to 1 are shown from top to bottom.

where \mathbf{U} and \mathbf{V} are the response and forcing modes, respectively, and Σ denotes the resolvent gain. The RESPOD forcing mode is projected onto the forcing modes of the modified resolvent operator and then amplified by the resolvent gains to generate the acoustic response whose spatial organisation is defined by the response modes. It was reported in Jeun *et al.* (2016) and later in Bugeat *et al.* (2022) that the forcing modes of the acoustic resolvent operator, $\tilde{\mathbf{R}}$, take the shape of streamwise supersonic waves with almost constant radial support. This indicates that the radially thin supersonic wavepackets observed in figure 8 are simply integrated in the radial direction as they are projected onto the forcing modes, which implies that the forcing modes of figure 8 can be replaced by a line source obtained by radial integration, justifying the use of line-source models in the literature (Michalke 1970; Michel 2009; Lesshafft *et al.* 2010; Cavalieri *et al.* 2011; Cavalieri & Agarwal 2014; Maia *et al.* 2019; da Silva *et al.* 2019). The resulting line sources at different frequencies are shown in figure 11 for the case M04Mc00. We observe wavepackets spanning $x/D = [0, 20]$ with a dominant wavenumber at all frequencies.

To characterise these wavepackets, we perform a FT in the streamwise direction. The amplitude and phase of the Fourier coefficients are shown in figure 12 for a range of frequencies. The wavenumber has been scaled by c_∞/ω so that the abscissa in the figure is the inverse phase speed, with the range $[-1, 1]$ corresponding to the supersonic phase speeds. We see the same peak corresponding to a phase speed, $c_x = 1.1722c_\infty$ at all frequencies, with energy contained in the immediate neighboring wavenumbers as well. The ordinate of the figure is scaled with St , and the peak has a nearly constant amplitude under this scaling. We ignore the rest of the spectrum and investigate the phase relation between this peak and

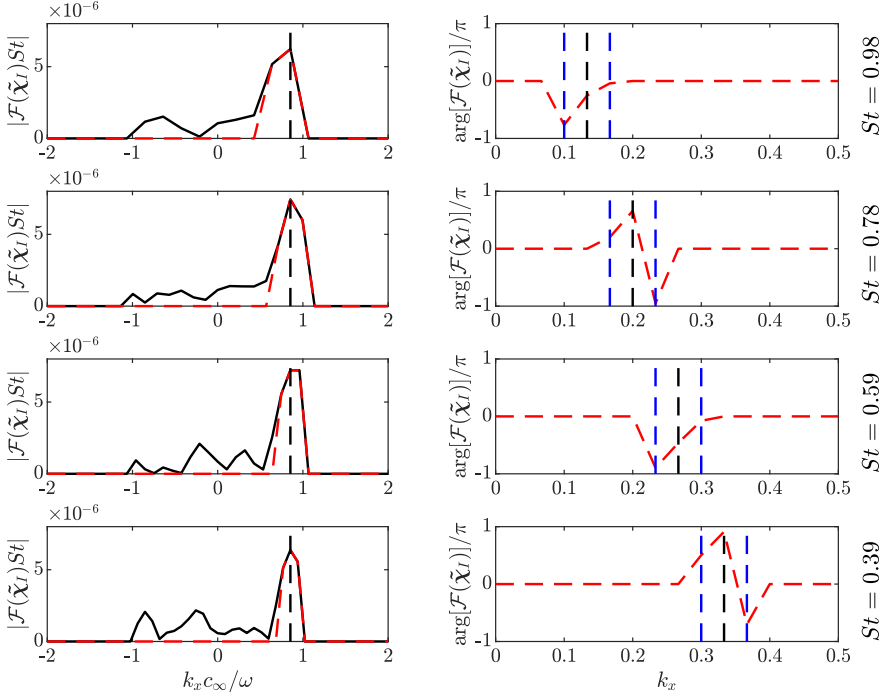


Figure 12: Amplitude (left) and phase (right) of the streamwise FT of the integrated line source. Red dashed line shows the isolated spectrum used for modelling. Vertical dashed black lines indicate the phase speed, $c_x = 1.1722c_\infty$, and dashed blue lines mark the neighbouring wavenumbers to that. Different frequencies ranging from $St = 0.4$ to 1 are shown from top to bottom.

the neighboring wavenumbers only, as shown in figure 12. There exists a phase difference of $\sim 0.5\pi$ between the central and leftmost wavenumbers. The phase difference between the central and rightmost wavenumbers is either around -1.7π or around 0.3π , which correspond to the same phase shift as $0.3\pi = \text{mod}(-1.7\pi, 2\pi)$.

Given these observations, we need to find a model consisting of three wavenumbers, the wavenumber corresponding to the constant phase speed observed and the neighbouring ones, with some empirical phase and amplitude relations in between and a global amplitude which scales with St . We propose the following empirical model,

$$\mathcal{F}_x(\xi) = \frac{A}{St} \left(e^{i\pi k_x^p} + B \left(e^{\phi_1 i \pi k_x^{p^-}} + e^{\phi_2 i \pi k_x^{p^+}} \right) \right), \quad (5.2)$$

where $A = 4.6 \times 10^{-7}$, $B = 0.8$, $\phi_1 = 0.5$, $\phi_2 = -0.7$, $k_x^p = St/(\beta c_\infty)$ is the wavenumber corresponding to the peak observed in figure 12 with $\beta = 1.1722$, and $k_x^{p^\pm}$ denotes the neighboring wavenumbers with $\Delta k_x = 1/30$ where 30 is the domain length. The corresponding forcing model, ξ , can then be obtained by taking the inverse FT of (5.2) in x . Note that the neighboring wavenumbers provide the wavepacket amplitude envelope without having to define a Gaussian-like form. Choosing a different domain length would change Δk_x , and therefore the resulting forcing model. But we anticipate that the results are not sensitive to this parameter, which will be justified later when showing the results for models at higher Mach numbers using the same value for L . Figure 13 shows a comparison of the forcing model obtained from (5.2) and the line source obtained from the LES data.

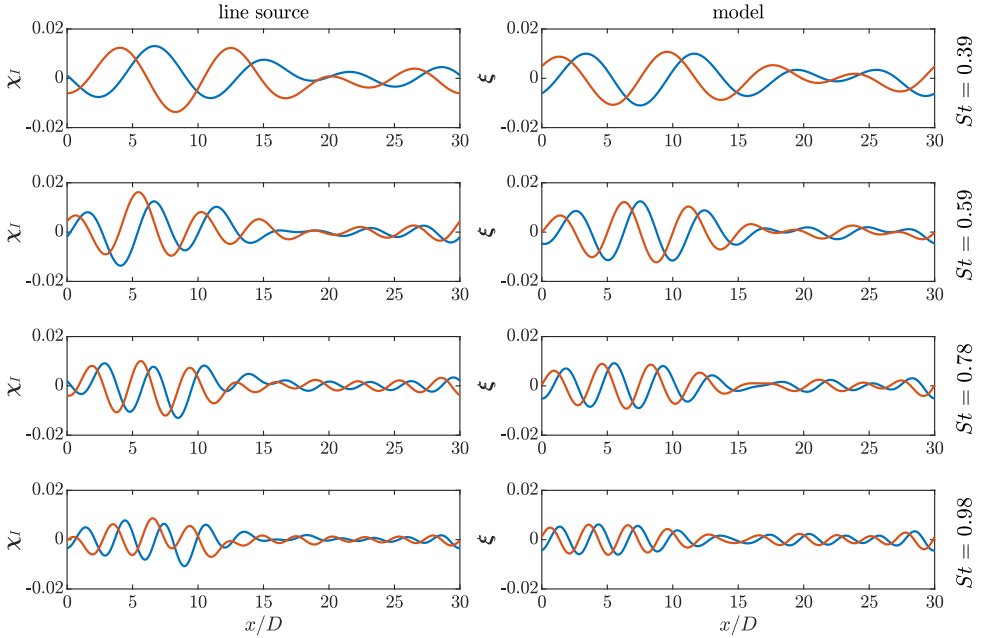


Figure 13: Real (blue) and imaginary (orange) parts of the line source (left) compared to the line-source model given by (5.2) (right). Different frequencies ranging from $St = 0.4$ to 1 are shown from top to bottom.

The model has a similar spatial support and the same dominant wavelength corresponding to the line source.

We now compare the acoustic response generated by this model to the response of the first RESPOD mode of the forcing, $\chi^{(1)}$, in figure 14 for a range of frequencies. The model accurately predicts downstream noise generation for high frequencies while it yields an underprediction at lower frequencies. The sound directivity is seen to be well captured at all frequencies, which implies that the underprediction at low frequencies can be fixed by adding a tuning parameter to the model. In the following section, we apply corrections to the model using acoustic data to improve predictions and to include Mach-number and flight effects.

5.2. Tuning the model using acoustic data from the LES

We discussed earlier that the errors in the LES database cause the correlation between the forcing and the acoustic field to be partially contaminated, yielding the response generated by the first RESPOD forcing mode, $\chi^{(1)}$, to globally underpredict the optimal SPOD mode of the acoustic field. As the forcing model in (5.2) is constructed based on the supersonic part of this forcing mode, the effect of the errors in the database is inherited in the model, ξ . To minimise this effect, we tune the model using the acoustic data obtained directly from the LES.

We start tuning the model, ξ by adding a scalar correction to better match the optimal SPOD mode of the acoustic field. In figure 15, the energy ratio of the response generated by the model, ξ , is compared with that of the optimal SPOD mode of the acoustic pressure as a function of frequency. Normalization is done using the total acoustic energy in the downstream region. It is seen that the underprediction of the model increases as the frequency

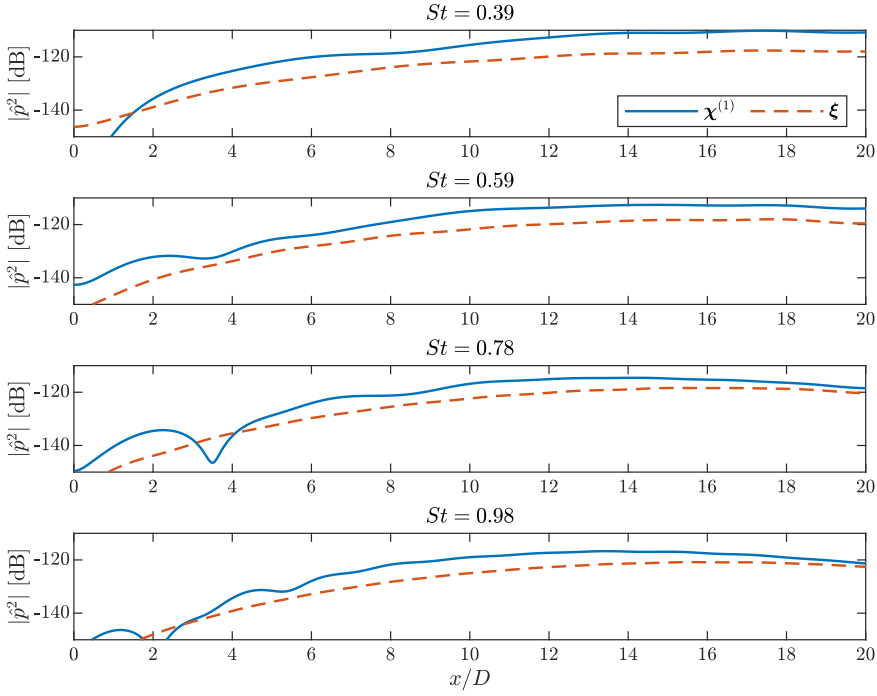


Figure 14: PSD of the acoustic pressure generated by the first RESPOD mode of the forcing (solid) compared to that of the line-source model (dashed) for the case M04Mc00. Different frequencies ranging from $St = 0.4$ to 1 are shown from top to bottom.

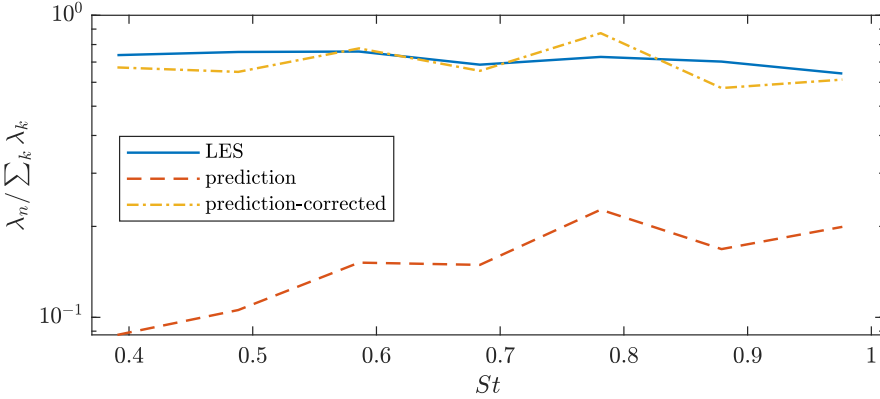


Figure 15: Energy ratio of the response generated by the line-source model (dashed) compared to that in the optimal SPOD mode of the acoustic pressure (solid). The energy ratio obtained using the corrected model is also shown (dash-dotted). Normalisations are done using the acoustic energy in the downstream region at each frequency.

decreases. A correction in the amplitude and changing the St^{-1} scaling to $St^{-3/2}$ yields the corrected trend seen in figure 15.

We now test the ansatz (5.2) to see if it can capture the Mach-number effect. The phase difference between k_x^P and k_x^{P-} mainly determines the shape of the envelope of the wavepacket while the phase difference between k_x^P and k_x^{P+} determines its streamwise position. It was

also found that the resulting acoustic field does not strongly depend on the value of B . Given these observations, we set β , A , ϕ_2 as free parameters to tune, and we keep ϕ_1 fixed to keep the wavepacket shape unchanged.

Assuming that the parameter β varies linearly with the jet Mach number M_j and matching the observed value at $M_j = 0.4$ and the observed phase velocity at $M_j = 0.9$ yields the expression

$$\beta = 0.7722 + M_j. \quad (5.3)$$

For $M_j = 0.9$, this results in a propagation angle of 53.3° , very close to the value observed by Bugeat *et al.* (2022).

To set the amplitude, A , and the phase constant, ϕ_2 , we performed tests to find the parameters that best match the acoustic field in the case M09Mc00. We finally obtained the empirical relations

$$A = 3.22 \times 10^{-6} M_j^{7/2}, \quad (5.4)$$

$$\phi_2 = 0.1 - St. \quad (5.5)$$

The resulting model equation with these corrections reads

$$\mathcal{F}_x(\xi) = 3.15 \times 10^{-6} \sqrt{\frac{M_j^7}{St^3}} \left(e^{i\pi k_x^p} + B \left(e^{0.5i\pi k_x^{p-}} + e^{(0.1-St)i\pi k_x^{p+}} \right) \right), \quad (5.6)$$

where

$$k_x^p = \frac{St}{(0.7722 + M_j)c_\infty}, \quad (5.7)$$

and $k_x^{p\pm}$ denotes once again the neighboring wavenumbers with $\Delta k_x = 1/30$. The resulting acoustic field is shown in figure 16 for M04Mc00 and M09Mc00 and compared to the corresponding LES data. It is seen that the model given in (5.6) yields a prediction that well matches the LES data in the downstream region at all frequencies. The acoustic response does not noticeably differ for the case M04Mc00 whether one uses a constant or linearly varying value for the phase, ϕ_2 .

Finally, we extend the empirical model given in (5.6) to take into account the flight effect. It is known that the effect of flight is to suppress noise, largely due to the suppression of turbulence in the shear layer (Maia *et al.* 2022). We compare the noise generated in the cases M09Mc00, M09Mc15 and M09Mc30, respectively, in figure 17 with two different scalings. Defining,

$$k_I(M_j, M_\infty) = \int_S K(M_j, M_\infty) dS, \quad (5.8)$$

where $K(M_j, M_\infty)$ denotes the turbulent kinetic energy as a function of the jet Mach number, M_j , and the flight Mach number, M_∞ , and using the scaling k_I^2 causes the sidestream noise in the three cases to collapse on top of each other. The dominant terms in the forcing have the form $\mathbf{u} \cdot \nabla \mathbf{u}$, which has the same dimension with turbulent kinetic energy differentiated in space. Inspired from this, we defined a scaling factor using $\partial_x K$ as

$$k_{I,x}(M_j, M_\infty) = \int_S \partial_x K(M_j, M_\infty) dS. \quad (5.9)$$

The scaling $k_{I,x}^2$ yields a slightly improved match in the peak noise level of the three cases. To determine if this scaling should be directly adopted in the forcing model, one needs to

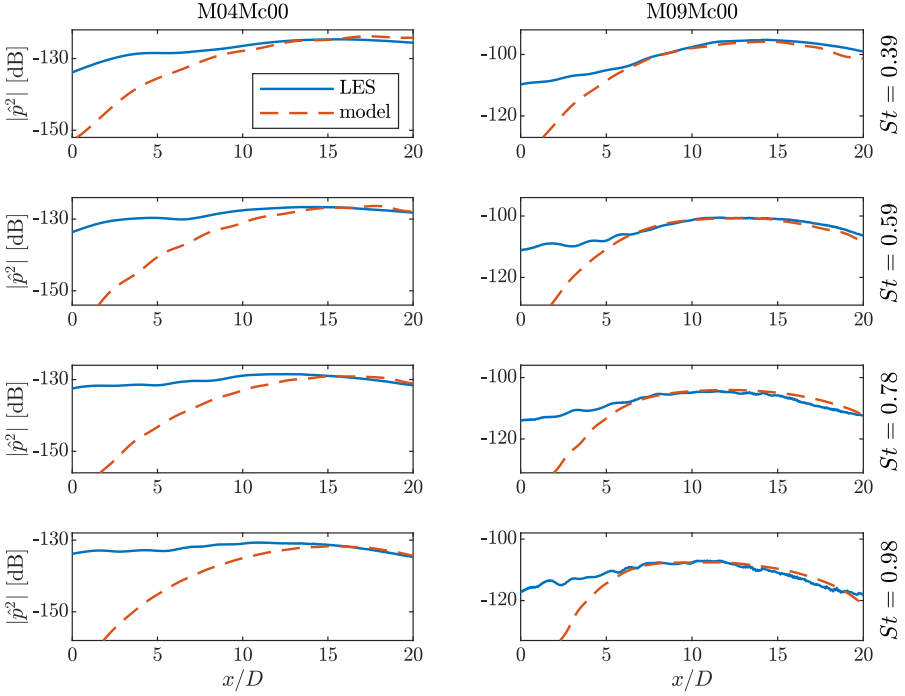


Figure 16: PSD of the acoustic pressure obtained using line-source model (5.6) to that extracted from the LES for the cases M04Mc00 (left) and M09Mc00 (right). Different frequencies ranging from $St = 0.4$ to 1 are shown from top to bottom.

understand the effect of the free stream on the efficiency of the noise generation mechanisms embedded in the resolvent operator. For this, we performed a resolvent-based noise prediction using the same forcing in the three cases at $M_j = 0.9$. The resulting acoustic fields are shown in figure 18, where it is seen that the change in the mean flow does not strongly affect noise level, but causes a change in the directivity in a similar fashion as observed in the LES data seen in figure 17. This suggests that one may use the same mathematical form for the source model for jets with or without flight effect, applying an amplitude correction. We adopt $k_{I,x}^2$ scaling for the empirical model as the peak noise, which occurs in the downstream region, is more relevant for the present study. Besides the amplitude correction, comparison of the model prediction with the LES data with flight stream effect yielded that the phase constant, ϕ_2 , is to be updated as

$$\phi_2 = 0.1 - St \frac{M_j - M_\infty}{M_j}, \quad (5.10)$$

resulting in the final equation for the jet-noise source model,

$$\mathcal{F}_x(\xi) = 3.15 \times 10^{-6} \Gamma \sqrt{\frac{M_j^7}{St^3}} \left(e^{i\pi k_x^p} + B \left(e^{0.5i\pi k_x^{p-}} + e^{(0.1 - St(M_j - M_\infty)/M_j)i\pi k_x^{p+}} \right) \right), \quad (5.11)$$

where

$$\Gamma \triangleq \frac{k_{I,x}(M_j, M_\infty)}{k_{I,x}(M_j, 0)}. \quad (5.12)$$

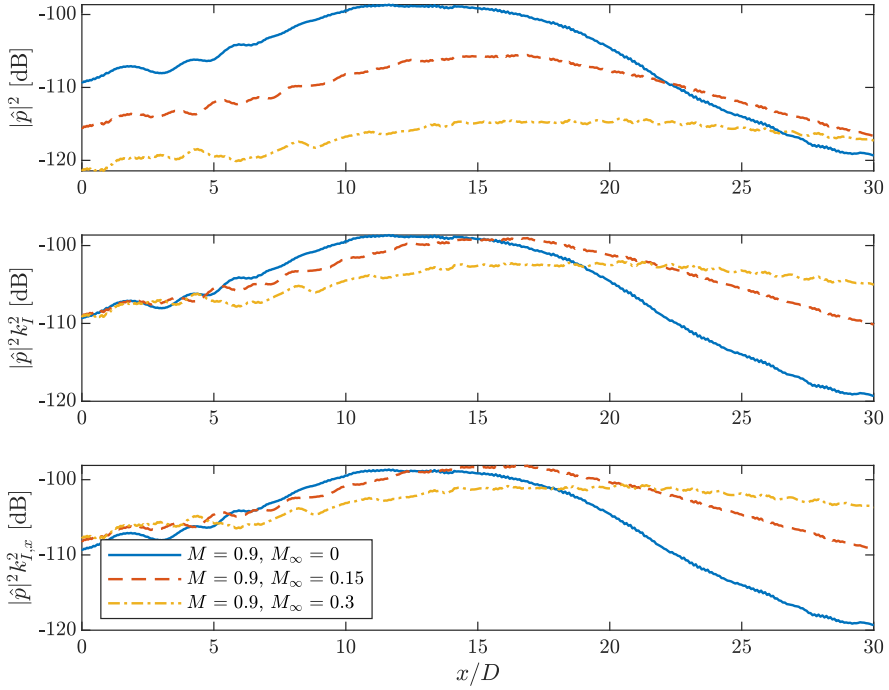


Figure 17: PSD of the acoustic pressure for the cases M09Mc00 (solid), M09Mc15 (dashed) and M09Mc30 (dash-dotted) with no scaling (top), k_I^2 scaling (center) and $k_{I,x}^2$ scaling (bottom) at $St = 0.6$.

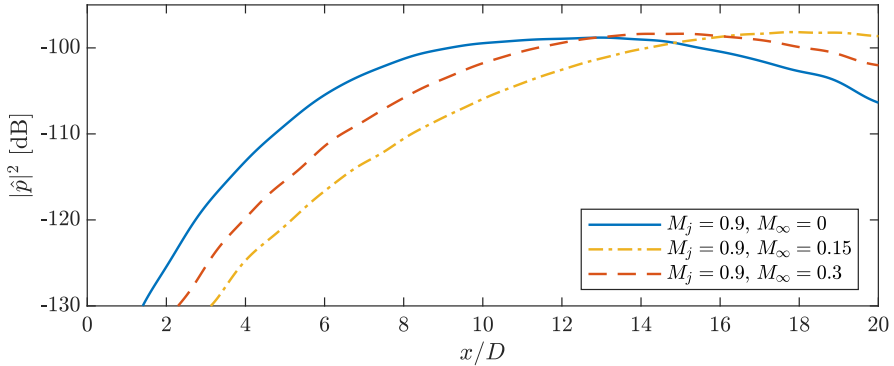


Figure 18: PSD of the acoustic pressure obtained using the line-source model given in (5.6) for the cases M09Mc00 (solid), M09Mc15 (dashed) and M09Mc30 (dash-dotted) at $St = 0.6$.

The resulting acoustic response of the model forcing obtained by taking the inverse FT of (5.11) is compared to the acoustic fields coming from the LES data in the cases M09Mc15 and M09Mc30, respectively, in figure 19. The error at all the frequencies remains within 2dB for the downstream region.

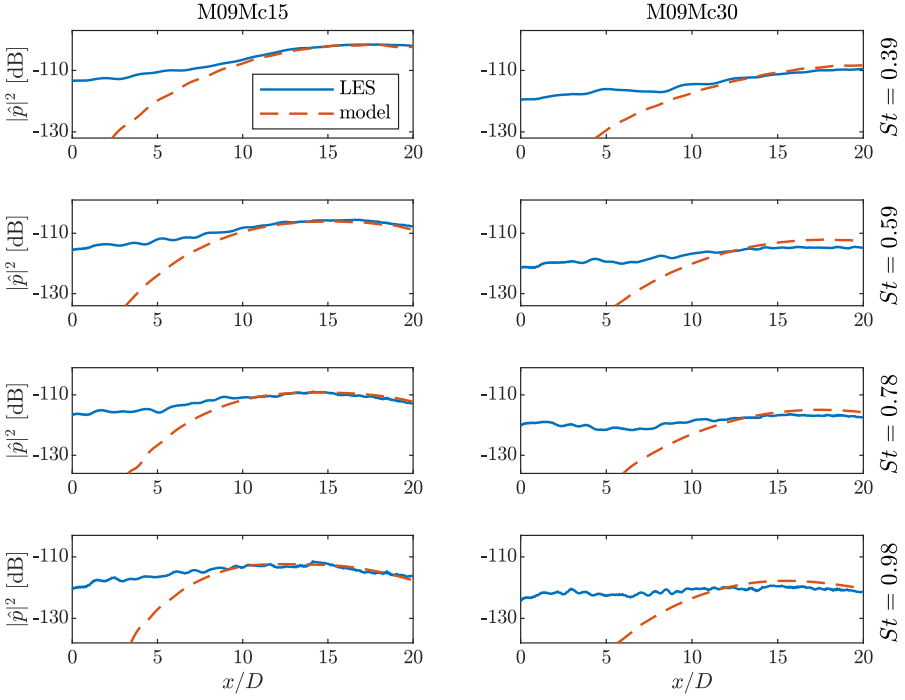


Figure 19: PSD of the acoustic pressure obtained using the line-source model given in (5.11) (dashed) compared to the LES data (solid) for the cases M09Mc15 (left) and M09Mc30 (right). Different frequencies ranging from $St = 0.4$ to 1 are shown from top to bottom.

5.3. Blind testing the model under different operating conditions

To test the validity of the model given in (5.11), we use three LES cases that were not used in its development: M07Mc00, M07Mc015 and M08Mc00 (see table 1 for details). The predictions are compared against the LES data in figure 20. The acoustic response generated by the forcing model predicts the downstream acoustic field with a 1dB accuracy within the region $x/D = [10, 20]$ for the static jets at $M_j = 0.7$ and 0.8, except for a sharper decay observed at $St = 1$ beyond $x = 19D$ for both cases. For the case with flight effect, the peak noise level is predicted accurately at all the frequencies. The accuracy of the prediction is within 2 dB for the region $x/D = [10, 20]$ at $St = 0.4$ and 0.6 and for the region $x/D = [12, 20]$ at $St = .8$. A sharper decay is observed for $St = 1$ at $x = 14D$. These results show that the proposed forcing model is capable of predicting jet noise within the Mach number and Strouhal number ranges $M_j = [0.4, 0.9]$ and $St = [0.4, 1]$, respectively. The suppression of jet noise due to flight effect is also well captured for the regime $M_\infty/M_j < 0.33$. Beyond these limits, the validity of the model remains to be tested.

Finally, we present a comparison of the model prediction and the LES data as a function of frequency in figure 21 for all the cases investigated in this study at two different propagation angles, $\theta = 15^\circ$ and 25° measured from the downstream end, which correspond to $x/D = 18.7$ and 10.7, respectively, in previous figures showing PSD data. The region $\theta < 25^\circ$ roughly determines the acoustic field dominated by the first RESPOD forcing mode and thus, the region of validity of the model. And $\theta = 15^\circ$ is near the sponge zone limit used in the resolvent

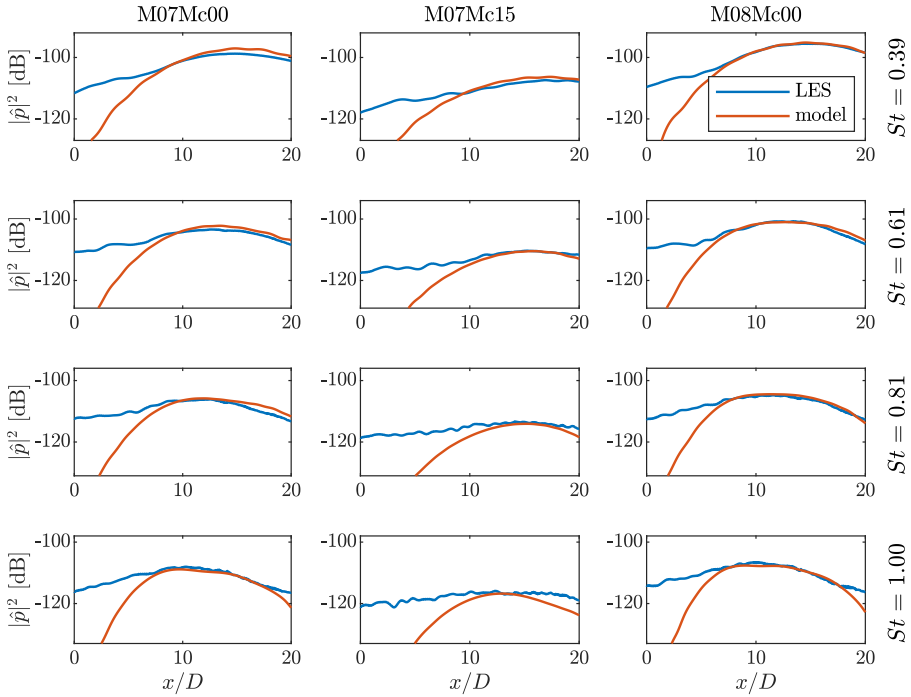


Figure 20: PSD of the acoustic pressure obtained using the line-source model given in (5.11) (dashed) compared to the LES data (solid) for the cases M07Mc00 (left), M07Mc15 (center) and M08Mc00 (right). Different frequencies ranging from $St = 0.4$ to 1 are shown from top to bottom.

computations. The frequency range in this comparison is extended to $St = [0.1, 1.5]$ to show the model performance beyond the range it has been tuned for. We limit the analysis to this range since, below $St = 0.1$, the hydrodynamic fluctuations reaches the acoustic field as reported by Nekkanti & Schmidt (2021) who used the same database for the cases M09Mc00 and M07Mc00; and at $St = 1.5$, the acoustic level is already 20 dB less than the peak in all the cases.

For the range $St = [0.4, 1]$, the model accurately predicts the acoustic field for all the cases, despite some underestimation for the cases M04Mc00, M07Mc15 and M09Mc30 at $\theta = 25^\circ$. But at slightly lower propagation angles, the model starts to yield better predictions for these three cases as well, as can be seen in figures 16, 19 and 20. At $St = 1.5$, the model yields accurate predictions in all the cases except for the cases M07Mc00 and M08Mc00 at $\theta = 15^\circ$. At frequencies below $St = 0.4$, the model starts to overpredict the acoustic level which becomes evident at $St = 0.1$ in all the cases. We expect the model to be valid only above a certain frequency, the forcing amplitude is scaled by $1/St^{3/2}$ in (5.11), which tends to infinity as $St \rightarrow 0$. The overprediction remains within 3 dB at $St = 0.2$ for all the cases except M07Mc00, M07Mc15 and M09Mc30, where it reaches up to 5 dB. Another reason that may explain the poor performance at low frequencies is that the identity of the leading resolvent mode switches from Kelvin-Helmholtz to Orr mechanism at around $St = 0.3$ (Pickering *et al.* 2020), and the very different physics of Orr modes would require a different forcing model.

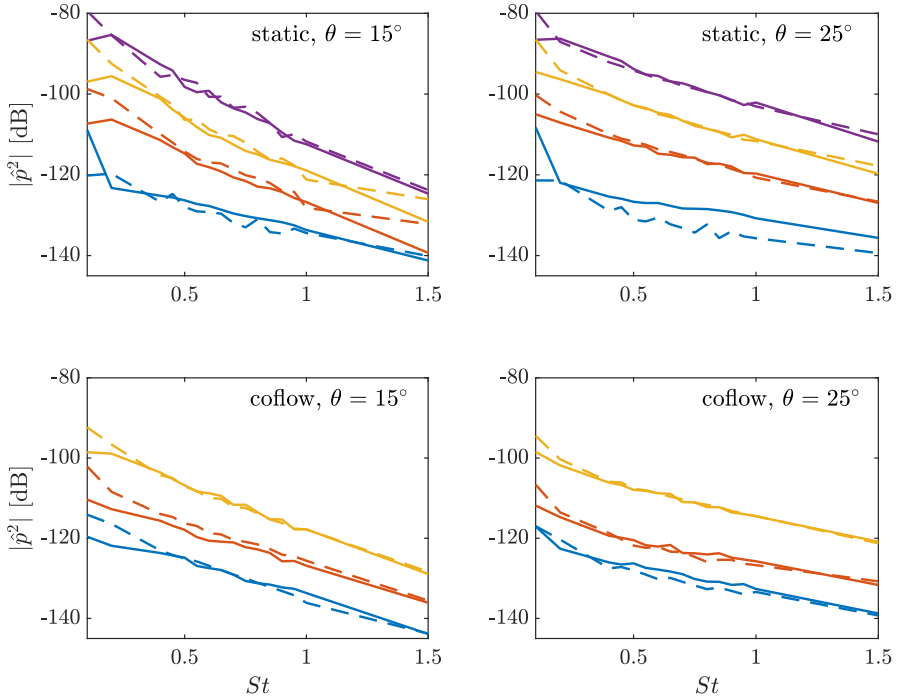


Figure 21: PSD of the acoustic pressure obtained from LES (solid) and predicted by the line-source model (dashed) for static jet cases (top) and cases with flight stream (bottom) at two different propagation angles, $\theta = 15^\circ$ (left) and 25° (right).

5.4. Discussion on the empirical modelling

We have presented a rank-1 model for acoustic sources in subsonic jets, defined within the resolvent framework. The overall prediction involves mean flow and turbulent kinetic energy data, which can be obtained from a RANS solution. It is known that there is a strong connection between the wavepackets found in the jet near field and the noise in the acoustic field (Cavaliere *et al.* 2012). It is therefore reasonable to assume that the forcing responsible for noise generation emerges from the nonlinear interaction of different wavepackets in the jet. The accuracy of the predictions implies that our model successfully incorporates the essential information from these wavepacket interactions to generate the downstream noise. The model consists of forcing structures with supersonic phase speeds determined by shifting the jet Mach number by a constant value. Such structures with supersonic phase speeds in subsonic jets are potentially a product of (i) spatial modulation of the convected waves due to the shape of the wavepacket, yielding a supersonic tail in the wavenumber domain (Crighton 1975; Tam *et al.* 2008; Jordan & Colonius 2013), or (ii) jittering in the wavepackets, which manifests in the frequency domain as coherence decay, causing a shift in the energy of the wavepacket towards supersonic wavenumbers (Cavaliere *et al.* 2011; Cavaliere & Agarwal 2014). Both model problems (Cavaliere & Agarwal 2014; Cavaliere *et al.* 2019) and real jet data (Maia *et al.* 2019; da Silva *et al.* 2019) have shown that the noise generated by a wavepacket in a subsonic jet is highly sensitive to the coherence decay rate embedded in the source model. Indeed, a source model based on a wavepacket with unit coherence, although matching the near-field wavepacket obtained experimentally, generates an acoustic field that

is off by up to 40 dB compared to the experimental data (Baqui *et al.* 2013; Jordan *et al.* 2014). This implies that the supersonic structures we observe in the forcing data are more likely to be associated with the coherence decay in the jet near field, and thus the jitter mechanism. Given this perspective, the model presented here can be considered to provide an indirect representation of the coherence decay occurring due to jittering in subsonic turbulent jets.

The present approach is based on the Mach-wave mechanism. Such a model is bound to be limited to low propagation angles, as the phase speed corresponding to 90° should tend to infinity for the same mechanism to be responsible for side stream propagation as well. However, we believe that a similar analysis based on resolvent framework can still be helpful in understanding the underlying mechanism for sidestream propagation in subsonic jets, which is left as a future task.

6. Conclusions

We outlined a methodology to identify the source of subsonic jet noise at low (downstream) propagation angles. Since noise generation by turbulent flows is nonlinear, it is not possible to uniquely define the source terms. Acoustic analogies (Lighthill (1952); Lilley (1974); Howe (1975); Doak (1995); Goldstein (2003); etc.) recast the Navier-Stokes (N-S) equations as a acoustic wave equation, with all other terms considered as the source. In this study, we instead adopt the resolvent framework, in which the linearized N-S equations serve as the operator and all nonlinear terms remaining after linearisation about the mean flow are viewed as the source terms, or *forcing*, in resolvent terminology.

Using the resolvent framework, we showed that downstream noise is generated mainly by the streamwise momentum forcing term. We then obtained a low-rank reconstruction of this forcing term using the RESPOD method (Towne *et al.* 2015; Karban *et al.* 2022a). The RESPOD method yields forcing modes that generates the SPOD modes of the measured response, which is selected to be the acoustic pressure in this study. The response modes are orthogonal to each other by construction. Searching for a similar orthogonality on the forcing side, we projected the RESPOD modes of the forcing onto streamwise harmonic waves with different phase velocities varying in the supersonic range, which yielded two critical outcomes: (i) projection coefficients corresponding to the first RESPOD mode of the forcing peaked around the same phase velocity at all the frequencies investigated; (ii) projection coefficients corresponding to the second RESPOD mode of the forcing showed a dip around the same phase velocity as a trace of the orthogonality in the response. Decomposing the first RESPOD mode of the forcing into supersonic and subsonic components, we demonstrated that it is the supersonic part of the forcing which generates the majority of the acoustic field in the downstream region.

The resolvent framework requires the mean flow data and the forcing model requires the turbulent kinetic energy, in case of non-zero flight stream. In this study, we obtained these data using the LES, which was shown to match the experimental data (Brès *et al.* 2018; Maia *et al.* 2022). One can alternatively obtain these performing a RANS simulation, which are then expected to be less accurate. The dependency of the model results on the turbulence models used in case of a RANS simulation, and on the accuracy of the first-order statistics in general is yet to be determined in a future study.

Given that the forcing modes of the acoustic resolvent operator, i.e., the resolvent operator that includes the measurement matrix that extracts the acoustic pressure as the response, supports a radially compact line source as the optimal forcing, we integrated the identified forcing in the radial direction, which yielded a wave packet with a dominant wavenumber corresponding to a constant phase velocity for all frequencies in the range $St = [0.4, 1]$. Using this information, we introduced a model equation for the line source. We tested the

line source for different flow cases with or without flight stream effects. Tuning the model by comparing the acoustic response it generated against the noise field extracted from the LES data resulted in a model in which the amplitude is scaled with $M_j^{7/2}$ and $St^{-3/2}$ and a linear phase relation is obtained changing with St and M_∞ . The model generates a noise field with an error of less than 2 dB in the downstream region in subsonic jets over a range of frequencies.

Identifying a dominant phase speed in the acoustically efficient forcing can be of practical importance beyond yielding a source model for noise generation in subsonic jets. One can investigate the interaction mechanisms that generate forcing components at this phase speed. Given the elongated wavepacket structure observed in the source, it is reasonable to assume that these structures are associated with interaction of certain wavepackets and may potentially be traced back in the nozzle, which may help to design strategies to control the jet noise. It was already shown in Maia *et al.* (2021) that real-time control in forced jets is possible by measuring the stochastic disturbances in the upstream region near the nozzle exit. The control practice becomes much harder in unforced jets due to loss of coherence between the actuators and the measurements. But this loss of coherence might be due to very poor signal-to-noise ratio in unforced jets. Our observation that the acoustically efficient forcing amounts to less than 0.04% of the total forcing energy for the $M_j = 0.4$ case supports this hypothesis. Extracting the structures at the dominant phase speed observed in the forcing in real-time by two-point measurements can significantly enhance the signal-to-noise ratio that is necessary for a successful control application.

Funding. This work has received funding from the Clean Sky 2 Joint Undertaking under the European Union’s Horizon 2020 research and innovation programme under grant agreement No 785303. U.K. has received funding from TUBITAK 2236 Co-funded Brain Circulation Scheme 2 (Project No: 121C061). A.T. was supported in part by ONR grant N00014-22-1-2561.

Declaration of interests. The authors report no conflict of interest.

Appendix A. Errors in the numerical database

To achieve accurate resolvent-based predictions of the response, the forcing and the response data should satisfy (2.3). Similarly, the RESPOD method assumes that the forcing and the response are connected to each other in the frequency domain via the resolvent operator as in (2.14). The LES database contains errors from several sources that cause the above conditions to be violated. Here, we briefly discuss here these error sources and their potential effect on the results.

The LES data is generated by solving the spatially filtered N-S equations. The forcing data, as discussed in §3.1, is obtained by computing the numerical Jacobian of this nonlinear LES operator to create a consistent forcing. The resolvent code, on the other hand, uses the linearised N-S equations without taking into account the filtering of the sub-grid scales implemented in the LES solver. This creates a compatibility issue when driving the resolvent operator with the forcing data obtained from the LES. Considering that the LES is sufficiently refined to capture the acoustic signature of the jet in an accurate way, we may assume that the differences between the LES and the N-S operators are small, at least for the scales we are interested in, and the sub-grid-scale filtering do not pose significant error in the database.

The LES data were first generated on an unstructured grid and then interpolated onto a cylindrical grid to facilitate azimuthal decomposition. Although the cylindrical grid has a distribution similar to that of the LES grid in streamwise and radial directions (Brès *et al.* 2017), interpolating the data stored in control volumes onto grid points causes interpolation errors in the data. Besides, the mesh used for the resolvent operator is not identical to

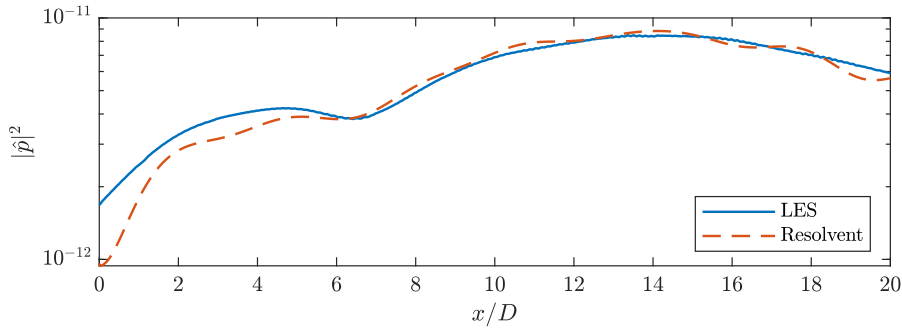


Figure 22: Comparison of the PSD of pressure extracted from LES and predicted via resolvent analysis at $r = 5D$ for the case M04Mc00 at $St = 0.6$.

the cylindrical grid used to store the LES data. The difference in the mesh requirement for the LES and the resolvent operator may vary, particularly at high frequencies, as the resolvent operator does not benefit from any sub-grid-scale filtering. Using a separate mesh for the resolvent operator requires an additional interpolation, introducing additional errors (although we expect that the errors due to this second interpolation are smaller compared to the first interpolation).

The LES data were stored with a temporal downsampling ratio of 200, yielding a sampling frequency, $St_s = 12.5$, for which the Nyquist limit to avoid aliasing is given as 6.25 (Nyquist 1928; Shannon 1948). A detailed analysis of the aliasing the LES database was given in Karban *et al.* (2022b), where it was shown that significant aliasing was observed in the forcing data even though it is negligible in the response. As resolvent analysis is performed in the frequency domain, aliasing appears as an error source for both forcing identification based on RESPOD and the resolvent-based prediction of the response.

These errors accumulate in the LES database. It is not possible to accurately quantify contributions from each error source, but one may use the difference between the state obtained directly from the LES and its prediction obtained using the resolvent tool as a global measure of the total error included in the database. In figure 22, we show a comparison of the PSD of the pressure in the acoustic field, i.e., at $r = 5D$, directly extracted from the LES data, and its resolvent-based prediction for the case M04Mc00 at $St = 0.6$. The acoustic field is predicted with reasonable accuracy, except the most upstream part, $x < 1D$, where the resolvent-based prediction suffers from a boundary condition effect. These error levels are similar to those observed by Towne *et al.* (2021) when comparing the PSD extracted from an LES database and obtained from a forced resolvent model for a supersonic jet. These results show that, although being contaminated by errors to a certain extent, the current database can be used to investigate noise generation mechanism in jets at this Mach number.

REFERENCES

- BALAY, S., GROPP, W. D., MCINNES, L. C. & SMITH, B. F. 1997 Efficient management of parallelism in object oriented numerical software libraries. In *Modern Software Tools in Scientific Computing*, pp. 163–202. Birkhäuser Press.
- BAQUI, Y. B., AGARWAL, A., CAVALIERI, A. & SINAYOKO, S. 2013 Nonlinear and linear noise source mechanisms in subsonic jets. In *19th AIAA/CEAS Aeroacoustics Conference*, arXiv: <https://arc.aiaa.org/doi/pdf/10.2514/6.2013-2087>.
- BECHARA, W., BAILLY, C., LAFON, P. & CANDEL, S. M. 1994 Stochastic approach to noise modeling for free turbulent flows. *AIAA Journal* **32** (3), 455–463, arXiv: <https://doi.org/10.2514/3.12008>.

- BENEDDINE, S., SIPP, D., ARNAULT, A., DANDOIS, J. & LESSHAFFT, L. 2016 Conditions for validity of mean flow stability analysis. *Journal of Fluid Mechanics* **798**, 485–504.
- BILLSON, M., ERIKSSON, L.-E., DAVIDSON, L. & JORDAN, P. 2004 Modeling of synthesized anisotropic turbulence and its sound emission. In *10th AIAA/CEAS Aeroacoustics Conference*, arXiv: <https://arc.aiaa.org/doi/pdf/10.2514/6.2004-2857>.
- BORÉE, J. 2003 Extended proper orthogonal decomposition: a tool to analyse correlated events in turbulent flows. *Experiments in fluids* **35** (2), 188–192.
- BRÈS, G., HAM, F., NICHOLS, J. & LELE, S. 2017 Unstructured large-eddy simulations of supersonic jets. *AIAA Journal* **55** (4), 1164–1184.
- BRÈS, G. A., JORDAN, P., JAUNET, V., LE RALLIC, M., CAVALIERI, A. V. G., TOWNE, A., LELE, S. K., COLONIUS, T. & SCHMIDT, O. T. 2018 Importance of the nozzle-exit boundary-layer state in subsonic turbulent jets. *Journal of Fluid Mechanics* **851**, 83–124.
- BUGEAT, B., CHASSAING, J.-C., ROBINET, J.-C. & SAGAUT, P. 2019 3d global optimal forcing and response of the supersonic boundary layer. *Journal of Computational Physics* **398**, 108888.
- BUGEAT, B., KARBAN, U., AGARWAL, A., LESSHAFFT, L. & JORDAN, P. 2022 Resolvent modelling of jet noise: the need for forcing models. Under review.
- CABANA, M., FORTUNÉ, V. & JORDAN, P. 2008 Identifying the radiating core of lighthill's source term. *Theoretical and Computational Fluid Dynamics* **22** (2), 87–106.
- CAVALIERI, A. V., JORDAN, P., AGARWAL, A. & GERVAIS, Y. 2011 Jittering wave-packet models for subsonic jet noise. *Journal of Sound and Vibration* **330** (18), 4474–4492.
- CAVALIERI, A. V. G. & AGARWAL, A. 2014 Coherence decay and its impact on sound radiation by wavepackets. *Journal of Fluid Mechanics* **748**, 399–415.
- CAVALIERI, A. V. G., JORDAN, P., COLONIUS, T. & GERVAIS, Y. 2012 Axisymmetric superdirectivity in subsonic jets. *Journal of Fluid Mechanics* **704**, 388–420.
- CAVALIERI, A. V. G., JORDAN, P. & LESSHAFFT, L. 2019 Wave-Packet Models for Jet Dynamics and Sound Radiation. *Applied Mechanics Reviews* **71** (2), 020802.
- CRIGHTON, D. 1975 Basic principles of aerodynamic noise generation. *Progress in Aerospace Sciences* **16** (1), 31–96.
- CURLE, N. 1955 The influence of solid boundaries upon aerodynamic sound. *Proceedings of the Royal Society of London. Series A. Mathematical and Physical Sciences* **231**, 505–514.
- DOAK, P. E. 1995 Fluctuating total enthalpy as a generalized acoustic field. *Acoustical Physics* **41**, 677–685.
- FFOWCS WILLIAMS, J. E. 1963 The noise from turbulence convected at high speed. *Philosophical Transactions of the Royal Society of London. Series A, Mathematical and Physical Sciences* **255** (1061), 469–503, arXiv: <https://royalsocietypublishing.org/doi/pdf/10.1098/rsta.1963.0010>.
- FREUND, J. B. 2001 Noise sources in a low-reynolds-number turbulent jet at mach 0.9. *Journal of Fluid Mechanics* **438**, 277–305.
- GARNAUD, X., LESSHAFFT, L., SCHMID, P. J. & HUERRE, P. 2013 The preferred mode of incompressible jets: linear frequency response analysis. *Journal of Fluid Mechanics* **716**, 189–202.
- GOLDSTEIN, M. E. 2003 A generalized acoustic analogy. *Journal of Fluid Mechanics* **488**, 315–333.
- GOLDSTEIN, M. E. & LEIB, S. J. 2008 The aeroacoustics of slowly diverging supersonic jets. *Journal of Fluid Mechanics* **600**, 291–337.
- GRYZEV, V., MARKESTEJN, A. P. & KARABASOV, S. A. 2022 Generalized acoustic analogy modeling of hot jet noise. *AIAA Journal* **60** (4), 2383–2396, arXiv: <https://doi.org/10.2514/1.J060896>.
- HOWE, M. S. 1975 Contributions to the theory of aerodynamic sound, with application to excess jet noise and the theory of the flute. *Journal of Fluid Mechanics* **71** (4), 625–673.
- HUERRE, P. & CRIGHTON, D. 1983 *Sound generation by instability waves in a low Mach number jet*, arXiv: <https://arc.aiaa.org/doi/pdf/10.2514/6.1983-661>.
- HWANG, Y. & COSSU, C. 2010 Amplification of coherent streaks in the turbulent couette flow: an input–output analysis at low reynolds number. *Journal of Fluid Mechanics* **643**, 333–348.
- JEUN, J., NICHOLS, J. W. & JOVANOVIĆ, M. R. 2016 Input-output analysis of high-speed axisymmetric isothermal jet noise. *Physics of Fluids* **28** (4), 047101, arXiv: <https://doi.org/10.1063/1.4946886>.
- JORDAN, P. & COLONIUS, T. 2013 Wave packets and turbulent jet noise. *Annual Review of Fluid Mechanics* **45** (1), 173–195.
- JORDAN, P., COLONIUS, T., BRÈS, G. A., ZHANG, M., TOWNE, A. & LELE, S. K. 2014 Modeling intermittent wavepackets and their radiated sound in a turbulent jet. In *Proceedings of the Summer Program*, pp. 241–249. Center for Turbulence Research, Stanford University.
- JUNG, D., GAMARD, S. & GEORGE, W. K. 2004 Downstream evolution of the most energetic modes in a

- turbulent axisymmetric jet at high reynolds number. part 1. the near-field region. *Journal of Fluid Mechanics* **514**, 173–204.
- KARABASOV, S. A., AFSAR, M. Z., HYNES, T. P., DOWLING, A. P., McMULLAN, W. A., POKORA, C. D., PAGE, G. J. & McGUIRK, J. J. 2010 Jet noise: Acoustic analogy informed by large eddy simulation. *AIAA Journal* **48** (7), 1312–1325, arXiv: <https://doi.org/10.2514/1.44689>.
- KARBAN, U., BUGEAT, B., MARTINI, E., TOWNE, A., CAVALIERI, A. V. G., LESSHAFFT, L., AGARWAL, A., JORDAN, P. & COLONIUS, T. 2020 Ambiguity in mean-flow-based linear analysis. *Journal of Fluid Mechanics* **900**, R5.
- KARBAN, U., MARTINI, E., CAVALIERI, A., LESSHAFFT, L. & JORDAN, P. 2022a Self-similar mechanisms in wall turbulence studied using resolvent analysis. *Journal of Fluid Mechanics* **939**, A36.
- KARBAN, U., MARTINI, E., JORDAN, P., BRÈS, G. A. & TOWNE, A. 2022b Solutions to aliasing in time-resolved flow data.
- LAFITTE, A., GARREC, T. L., LAURENDEAU, E. & BAILLY, C. 2011 A study based on the sweeping hypothesis to generate stochastic turbulence. In *17th AIAA/CEAS Aeroacoustics Conference (32nd AIAA Aeroacoustics Conference)*, arXiv: <https://arc.aiaa.org/doi/pdf/10.2514/6.2011-2888>.
- LANDAHL, M. T. 1967 A wave-guide model for turbulent shear flow. *Journal of Fluid Mechanics* **29** (3), 441–459.
- LEIB, S. J. & GOLDSTEIN, M. E. 2011 Hybrid source model for predicting high-speed jet noise. *AIAA Journal* **49** (7), 1324–1335, arXiv: <https://doi.org/10.2514/1.J050707>.
- LESSHAFFT, L., HUERRE, P. & SAGAUT, P. 2010 Aerodynamic sound generation by global modes in hot jets. *Journal of Fluid Mechanics* **647**, 473–489.
- LESSHAFFT, L., SEMERARO, O., JAUNET, V., CAVALIERI, A. V. G. & JORDAN, P. 2019 Resolvent-based modeling of coherent wave packets in a turbulent jet. *Phys. Rev. Fluids* **4**, 063901.
- LIGHTHILL, M. J. 1952 On sound generated aerodynamically i. general theory. *Proceedings of the Royal Society of London. Series A. Mathematical and Physical Sciences* **211** (1107), 564–587.
- LILLEY, G. M. 1974 On the noise from jets. *AGARD CP-131* pp. 13–1.
- LUMLEY, J. L. 1970 Toward a turbulent constitutive relation. *Journal of Fluid Mechanics* **41** (2), 413–434.
- MAIA, I. A., BRÈS, G., LESSHAFFT, L. & JORDAN, P. 2022 The effect of a flight stream on subsonic turbulent jets.
- MAIA, I. A., JORDAN, P., CAVALIERI, A. V. G. & JAUNET, V. 2019 Two-point wavepacket modelling of jet noise. *Proceedings of the Royal Society A: Mathematical, Physical and Engineering Sciences* **475** (2227), 20190199, arXiv: <https://royalsocietypublishing.org/doi/pdf/10.1098/rspa.2019.0199>.
- MAIA, I. A., JORDAN, P., CAVALIERI, A. V. G., MARTINI, E., SASAKI, K. & SILVESTRE, F. J. 2021 Real-time reactive control of stochastic disturbances in forced turbulent jets. *Phys. Rev. Fluids* **6**, 123901.
- MARTINI, E., CAVALIERI, A. V., JORDAN, P. & LESSHAFFT, L. 2019 Accurate frequency domain identification of odes with arbitrary signals. *arXiv: Signal Processing*.
- McKEON, B. J. & SHARMA, A. S. 2010 A critical-layer framework for turbulent pipe flow. *Journal of Fluid Mechanics* **658**, 336–382.
- MICHALKE, A. 1970 A wave model for sound generation in circular jets. *Tech. Rep.*. Deutsche Forschungs- und Versuchsanstalt für Luft- und Raumfahrt.
- MICHEL, U. 2009 The role of source interference in jet noise. In *15th AIAA/CEAS Aeroacoustics Conference (30th AIAA Aeroacoustics Conference)*, arXiv: <https://arc.aiaa.org/doi/pdf/10.2514/6.2009-3377>.
- MORRA, P., NOGUEIRA, P. A. S., CAVALIERI, A. V. G. & HENNINGSON, D. S. 2021 The colour of forcing statistics in resolvent analyses of turbulent channel flows. *Journal of Fluid Mechanics* **907**, A24.
- NEKKANTI, A. & SCHMIDT, O. T. 2021 Modal analysis of acoustic directivity in turbulent jets. *AIAA Journal* **59** (1), 228–239, arXiv: <https://doi.org/10.2514/1.J059425>.
- NOGUEIRA, P. A., CAVALIERI, A. V., JORDAN, P. & JAUNET, V. 2019 Large-scale streaky structures in turbulent jets. *Journal of Fluid Mechanics* **873**, 211–237.
- NOGUEIRA, P. A. S., MORRA, P., MARTINI, E., CAVALIERI, A. V. G. & HENNINGSON, D. S. 2021 Forcing statistics in resolvent analysis: application in minimal turbulent couette flow. *Journal of Fluid Mechanics* **908**, A32.
- NYQUIST, H. 1928 Certain topics in telegraph transmission theory. *Transactions of the American Institute of Electrical Engineers* **47** (2), 617–644.
- PHILLIPS, O. M. 1960 On the generation of sound by supersonic turbulent shear layers. *Journal of Fluid Mechanics* **9** (1), 1–28.
- PICARD, C. & DELVILLE, J. 2000 Pressure velocity coupling in a subsonic round jet. *International Journal of Heat and Fluid Flow* **21** (3), 359 – 364.

- PICKERING, E., RIGAS, G., NOGUEIRA, P. A. S., CAVALIERI, A. V. G., SCHMIDT, O. T. & COLONIUS, T. 2020 Lift-up, kelvin–helmholtz and orr mechanisms in turbulent jets. *Journal of Fluid Mechanics* **896**, A2.
- PICKERING, E., RIGAS, G., SCHMIDT, O. T., SIPP, D. & COLONIUS, T. 2021a Optimal eddy viscosity for resolvent-based models of coherent structures in turbulent jets. *Journal of Fluid Mechanics* **917**, A29.
- PICKERING, E., TOWNE, A., JORDAN, P. & COLONIUS, T. 2021b Resolvent-based modeling of turbulent jet noise. *The Journal of the Acoustical Society of America* **150** (4), 2421–2433, arXiv: <https://doi.org/10.1121/10.0006453>.
- POWELL, A. 1964 Theory of vortex sound. *The Journal of the Acoustical Society of America* **36** (1), 177–195, arXiv: <https://doi.org/10.1121/1.1918931>.
- SCHMIDT, O. T., TOWNE, A., RIGAS, G., COLONIUS, T. & BRÈS, G. A. 2018 Spectral analysis of jet turbulence. *Journal of Fluid Mechanics* **855**, 953–982.
- SHANNON, C. E. 1948 A mathematical theory of communication. *The Bell System Technical Journal* **27** (3), 379–423.
- SIEFERT, M. & EWERT, R. 2008 A stochastic source model for turbulent noise prediction including sweeping time dynamics. *The Journal of the Acoustical Society of America* **123** (5), 3129–3129, arXiv: <https://doi.org/10.1121/1.2933075>.
- DA SILVA, F. D., JORDAN, P. & CAVALIERI, A. V. G. 2019 On the modelling of wavepacket scattering noise with coherence effects. *The Journal of the Acoustical Society of America* **146** (6), 4472–4480, arXiv: <https://doi.org/10.1121/1.5140190>.
- SINAYOKO, S., AGARWAL, A. & HU, Z. 2011a Flow decomposition and aerodynamic sound generation. *Journal of Fluid Mechanics* **668**, 335–350.
- SINAYOKO, S., AGARWAL, A. & HU, Z. 2011b Flow decomposition and aerodynamic sound generation. *Journal of Fluid Mechanics* **668**, 335–350.
- TAM, C. K. W., VISWANATHAN, K., AHUJA, K. K. & PANDA, J. 2008 The sources of jet noise: experimental evidence. *Journal of Fluid Mechanics* **615**, 253–292.
- TINNEY, C. E., GLAUSER, M. N. & UKEILEY, L. 2008 Low-dimensional characteristics of a transonic jet. part 1. proper orthogonal decomposition. *Journal of Fluid Mechanics* **612**, 107–141.
- TOWNE, A. 2016 Advancements in jet turbulence and noise modeling: Accurate one-way solutions and empirical evaluation of the nonlinear forcing of wavepackets. PhD thesis, California Institute of Technology.
- TOWNE, A., BRÈS, G. A. & LELE, S. K. 2017 A statistical jet-noise model based on the resolvent framework. In *23rd AIAA/CEAS Aeroacoustics Conference*, arXiv: <https://arc.aiaa.org/doi/pdf/10.2514/6.2017-3706>.
- TOWNE, A., COLONIUS, T., JORDAN, P., CAVALIERI, A. V. & BRÈS, G. A. 2015 Stochastic and nonlinear forcing of wavepackets in a mach 0.9 jet. In *21st AIAA/CEAS Aeroacoustics Conference*.
- TOWNE, A., DAWSON, S., BRÈS, G. A., LOZANO-DURÁN, A., SAXTON-FOX, T., PARTHASARATHY, A., JONES, A. R., BILER, H., YEH, C.-A., PATEL, H. D. & OTHERS 2022 A database for reduced-complexity modeling of fluid flows. *arXiv:2206.11801* .
- TOWNE, A., LOZANO-DURÁN, A. & YANG, X. 2020 Resolvent-based estimation of space–time flow statistics. *Journal of Fluid Mechanics* **883**, A17.
- TOWNE, A., RIGAS, G., PICKERING, E. & COLONIUS, T. 2021 Efficient global resolvent analysis via the one-way Navier-Stokes equations. Part 1. Forced response. *arXiv:2111.09269* .
- TOWNE, A., SCHMIDT, O. T. & COLONIUS, T. 2018 Spectral proper orthogonal decomposition and its relationship to dynamic mode decomposition and resolvent analysis. *Journal of Fluid Mechanics* **847**, 821–867.
- YEH, C.-A. & TAIRA, K. 2019 Resolvent-analysis-based design of airfoil separation control. *Journal of Fluid Mechanics* **867**, 572 – 610.